Atomistic Modeling of Oxide Defects

Dominic Waldhoer, Al-Moatasem Bellah El-Sayed, Yannick Wimmer, Michael Waltl, and Tibor Grasser

1 Introduction

Random telegraph noise (RTN) refers to a stochastic discrete signal observed in the drain current I_D at a constant gate voltage V_G. This noise signal is believed to be caused by oxide defects, which can exchange charges with the device substrate or gate [1]. Charges trapped at oxide defects alter the device electrostatics, leading to a shift of the threshold voltage, denoted as ΔV_{th}. Since each discrete step in a random telegraph signal (RTS) stems from a single charge trapping/emission event of a specific defect, the analysis of these signals allows the experimental extraction of single-defect parameters. Typically, the impact of a single defect is only resolvable in small-area devices due to their small oxide capacitance. In contrast, large-area devices show a smooth ΔV_{th} degradation during operation at elevated temperatures and high gate voltages. This phenomenon is commonly known as bias temperature instability (BTI) [2] and is a serious reliability concern in modern MOSFET devices. It has been demonstrated in recent works that BTI and RTN are both linked to oxide defects and can therefore be modeled within the same framework [3]. Oxide defects can be either classified as hole traps or electron traps. In devices with a-SiO_2 dielectric, usually negative BTI (NBTI) caused by hole traps is the dominant degradation mechanism. In contrast, the increasing use of high-κ materials like HfO_2 also leads to significant positive BTI (PBTI) degradation, which is associated with electron traps in these materials [4].

D. Waldhoer (✉) · M. Waltl
Christian Doppler Laboratory for Single-Defect Spectroscopy in Semiconductor Devices, Institute for Microelectronics, Vienna, Austria
e-mail: waldhoer@iue.tuwien.ac.at; waltl@iue.tuwien.ac.at

A.-M. B. El-Sayed · Y. Wimmer · T. Grasser
Institute for Microelectronics, Vienna, Austria
e-mail: elsayed@iue.tuwien.ac.at; wimmer@iue.tuwien.ac.at; grasser@iue.tuwien.ac.at

© Springer Nature Switzerland AG 2020

T. Grasser (ed.), *Noise in Nanoscale Semiconductor Devices*,
https://doi.org/10.1007/978-3-030-37500-3_18

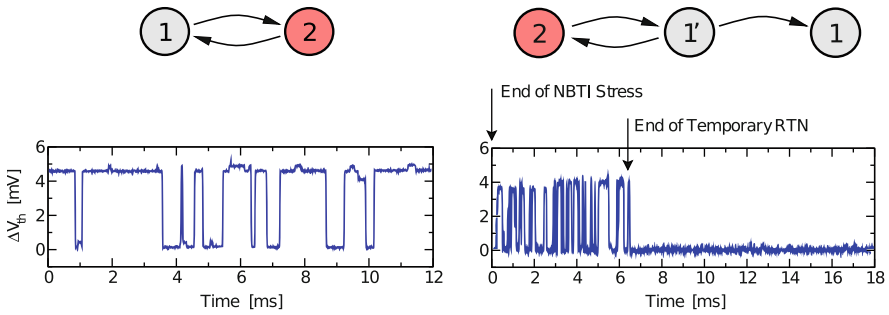

Fig. 1 RTN signals measured on a small-area pMOS. **Left:** A continuous RTN signal, which is produced by an oxide defect with two different states. **Right:** After BTI stress, often a so-called temporary RTN signal can be observed. In this case, the noise signal disappears after some time, indicating an additional electrically inactive defect state. Modified from [6]

Examples of frequently observed random telegraph signals are depicted in Fig. 1. The left figure shows a RTN signal produced by a two-state defect continuously switching between its two different charge states. The RTN signal of a fundamentally different defect is shown in Fig. 1 (right). In this case, the signal disappears after a certain time. This finding indicates a defect with at least three different states. The frequent occurrence of such signals in measurements lead to the development of the widely successful 4-state nonradiative multiphonon (NMP) model for the description of RTN and BTI [5, 6]. A brief review of this model is given in Sect. 4.

The various parameters of the 4-state NMP model can be fitted to data obtained from electrical defect characterization measurements. Techniques like RTS analysis [7] and time-dependent defect spectroscopy (TDDS) [8] allow the extraction of transition barriers and trap levels for individual defects. On the other hand the impact of a whole defect ensemble on device degradation can be monitored by applying measure-stress-measure (MSM) sequences [9]. A detailed description of experimental parameter extraction is given in Chapter 7 of this book [10]. Although these techniques allow for the electrical characterization of oxide defects, they can only provide limited information about the underlying physical and chemical nature of the defects. Using clean semiconductor-oxide samples instead of fully processed devices, additional insights into the atomistic structure of defects can be gained by electron spin resonance (ESR) spectroscopy. This technique is sensitive to defects with unpaired electrons. Using this method, various types of paramagnetic E′ centers were discovered in SiO_2 [11] as well as P_b centers at the Si/SiO_2 interface [12]. ESR measurements also confirmed the existence of hydrogenated E′ centers in amorphous SiO_2 [13]. Further experimental data also shows that hydrogen-related defects seem to play an important role for the RTN and NBTI phenomena in devices with SiO_2 gate dielectric [14–16].

Although all these experimental methods provide some information about the atomistic nature of oxide defects, a more detailed knowledge is desired in order to improve the device reliability and to justify and enhance existing reliability models.

In this context atomistic modeling provides a valuable tool to explore defects and their behavior theoretically. Over the last decades density functional theory (DFT) has become arguably the most popular ab-initio method in computational chemistry. Due to the ever increasing computational power in combination with the development of highly efficient algorithms, it has become feasible to simulate a collection of thousands of atoms quantum mechanically with DFT [17]. Even though the simulation of an entire device from first principles is still out of reach, it is possible to calculate defect parameters in bulk materials. In this chapter we will summarize the state-of-the-art methodology for point defect calculations using DFT. Furthermore we will review recent DFT results with an emphasis on hole traps in a-SiO_2 and electron traps in a-HfO_2, and compare them to experimental findings. It will be demonstrated that hydrogen-related defects like the hydrogen bridge (HB) or the hydroxyl-E′ center (H-E′) can act as hole traps in a-SiO_2 in agreement with NBTI and RTN measurements. PBTI in high-κ gate stacks on the other hand is likely caused by intrinsic electron traps in a-HfO_2.

2 DFT in a Nutshell

Atomistic modeling of materials has become an important tool in many fields of research. This approach allows the theoretical study of material properties like internal geometry, electronic structures, energy levels, or optical and vibrational absorption spectra just to name a few. The various methods of computational chemistry can be roughly separated in two groups, namely empirical and first principle (ab-initio) methods. Empirical approaches mostly assume an analytical force field between atoms and treat the resulting atomic movements entirely within classical mechanics. These methods are useful to determine geometric structures of molecules or solids. Empirical methods allow the study of very large molecules containing millions of atoms and are therefore very popular in biochemistry. However, these methods cannot give any information about the electronic structure of matter. For this task, ab-initio methods, which approximately solve the Schrödinger equation of the system, are needed. The study of defects, especially the estimation of their energy levels, therefore relies on ab-initio simulations. These approaches are computationally very expensive and scale considerably with the number of particles in the system, making them only usable for small molecules with just a handful of atoms. Among ab-initio methods, density functional theory (DFT) is arguably the most commonly used approach, due to its comparably low computational costs. DFT enables the quantum mechanical simulation of several thousand atoms on currently available computer hardware and is therefore very well suited for the study of defects in oxides. In the following we will give a brief introduction to general DFT. The modeling of amorphous structures and defects with DFT will be discussed later on.

2.1 Many-Body Schrödinger Equation

All non-relativistic properties of a system can, in principle, be determined by solving its time-independent many-body Schrödinger equation

$$\hat{H}\Psi\left(\tilde{\boldsymbol{r}}, \tilde{\boldsymbol{R}}\right) = E\Psi\left(\tilde{\boldsymbol{r}}, \tilde{\boldsymbol{R}}\right). \tag{1}$$

Here $\hat{H}$ represents the standard many-body Hamiltonian given by

$$\hat{H} = \hat{T}_n + \hat{T}_e + \hat{V} + \hat{U}\,, \tag{2}$$

which accounts for the kinetic energies of nuclei $\left(\hat{T}_n\right)$ and electrons $\left(\hat{T}_e\right)$, as well as the Coulomb interactions between nuclei and electrons $\left(\hat{V}\right)$ and between electrons themselves $\left(\hat{U}\right)$. The system's wavefunction Ψ is a function of all electronic and ionic coordinates, denoted by $\tilde{\boldsymbol{r}}$ and $\tilde{\boldsymbol{R}}$, respectively. A first common step in order to solve Eq. 1 is to assume a wavefunction, which is separable into an electronic wavefunction ψ and a vibrational wavefunction η

$$\Psi\left(\tilde{\boldsymbol{r}}, \tilde{\boldsymbol{R}}\right) = \psi\left(\tilde{\boldsymbol{r}}; \tilde{\boldsymbol{R}}\right)\eta\left(\tilde{\boldsymbol{R}}\right). \tag{3}$$

Electrons have a much lower mass than nuclei and can, therefore, be assumed to adapt to changes in the ionic coordinates $\tilde{\boldsymbol{R}}$ almost instantly. Applying this fact to the separation Ansatz Eq. 3 yields an electronic Schrödinger equation

$$\left(\hat{T}_e + \hat{V} + \hat{U}\right)\psi\left(\tilde{\boldsymbol{r}}; \tilde{\boldsymbol{R}}\right) = V\left(\tilde{\boldsymbol{R}}\right)\psi\left(\tilde{\boldsymbol{r}}; \tilde{\boldsymbol{R}}\right) \tag{4}$$

and a vibrational Schrödinger equation

$$\left(\hat{T}_n + V\left(\tilde{\boldsymbol{R}}\right)\right)\eta\left(\tilde{\boldsymbol{R}}\right) = E\eta\left(\tilde{\boldsymbol{R}}\right). \tag{5}$$

This approach is commonly known as the Born–Oppenheimer approximation [18]. Within this approximation the nuclei are assumed to move like classical particles in a potential $V\left(\tilde{\boldsymbol{R}}\right)$ generated by the electrons. This potential is referred to as potential energy surface (PES) and plays a central role in the description of defects within NMP theory as will be outlined in Sect. 4.

2.2 Hohenberg–Kohn Theorems

Ab-initio methods aim at solving the electronic Schrödinger equation (Eq. 4). This equation is exceptionally hard to solve due to the electron–electron interaction operator $\hat{U}$, which prohibits a separation in single-electron wavefunctions. In fact, even a numerical solution of the electronic equation without further physical

approximations is unfeasible even for small systems. One can approximate $\hat{U}$ by the interaction of each individual electron with the mean field caused by all electrons. This so-called Hartree–Fock (HF) method leads to Schrödinger equations of single electrons moving in an effective potential. These equations can be solved self-consistently for the single-electron wavefunctions. Although the HF method can produce a rough estimate of the electronic structure, it completely neglects electron correlation effects and is generally not accurate enough for practical calculations. The so-called post-HF methods like Møller–Plesset perturbation theory or the coupled cluster approach can mitigate these drawbacks at the price of greatly increased computational demands. Further details on HF and other wavefunction based methods can be found in [19].

When only the electronic ground state ψ_0 is of interest, a fundamentally different approach for solving Eq. 4 is offered by two important theorems proven by Hohenberg and Kohn [20]. These theorems establish a one-to-one mapping between the ground state electron density $n_0(\boldsymbol{r})$ and the ground state electronic wavefunction ψ_0, and can be stated as [21]:

1. The ground state wavefunction is a unique functional $\psi_0 = \psi[n_0]$ of the ground state electron density. As a consequence, every ground state observable $\hat{O}$ can be defined as a density functional as well

$$O[n_0] = \langle \psi[n_0] | \hat{O} | \psi[n_0] \rangle .$$

2. The energy functional $E[n]$ obtains its global minimum for the true ground state electron density n_0.

These theorems allow the reformulation of the many-body Schrödinger equation in terms of a variational problem with respect to the electron density $n(\boldsymbol{r})$. Therefore, instead of searching explicitly for the $3N$ dimensional wavefunction ψ_0, knowledge about the 3 dimensional electron density $n(\boldsymbol{r})$ is sufficient to derive all other ground state properties.

2.3 Kohn–Sham Equations

Although the Hohenberg–Kohn theorems provide a vast simplification of the problem at hand, they only prove the existence of a kinetic energy functional $T[n]$ and an electron interaction functional $U[n]$. However, these functionals are unknown for interacting electrons. In order to apply DFT to real systems, most often the method of Kohn–Sham (KS) orbitals [22] is employed. In this approach the electron density is assumed to be constructed by a set of non-interacting single-electron wavefunctions

$$n\left(\boldsymbol{r}\right) = \sum_{i=1}^{N_{\mathrm{el}}} \left|\phi_i\left(\boldsymbol{r}\right)\right|^2 . \tag{6}$$

For such a system of non-interacting electrons, the resulting kinetic energy is simply given by

$$T_{\mathrm{s}}[n] = -\frac{1}{2}\sum_{i=1}^{N_{\mathrm{el}}} \langle\phi_i|\nabla^2|\phi_i\rangle \ . \tag{7}$$

In classical electrodynamics the interaction functional can be expressed by the so-called Hartree-energy

$$U_{\mathrm{H}}\left[n\right] = \frac{1}{2}\iint \frac{n\left(\boldsymbol{r}\right) n\left(\boldsymbol{r'}\right)}{\left|\boldsymbol{r}-\boldsymbol{r'}\right|}\mathrm{d}^3\boldsymbol{r}\mathrm{d}^3\boldsymbol{r'}. \tag{8}$$

Although T_{s} and U_{H} do not account for the quantum mechanical exchange and correlation effects, they represent the largest contributions to the true functionals T and U. All the unknown quantum mechanical many-body effects are collected in a so-called exchange-correlation functional $E_{\mathrm{XC}}\left[n\right]$. The functional of the total energy can, therefore, be written as

$$E\left[n\right] = T_{\mathrm{s}}\left[n\right] + U_{\mathrm{H}}\left[n\right] + V\left[n\right] + E_{\mathrm{XC}}\left[n\right] \ . \tag{9}$$

Using the representation of the electron density by KS orbitals and applying the Euler–Lagrange formalism to Eq. 9 yields a system of eigenvalue problems for the individual orbitals, the so-called Kohn–Sham equations

$$\left(-\frac{1}{2}\nabla^2 + v_{\mathrm{eff}}\left(\boldsymbol{r}\right)\right)\phi_i\left(\boldsymbol{r}\right) = \epsilon_i\phi_i\left(\boldsymbol{r}\right). \tag{10}$$

These equations describe individual non-interacting electrons in an effective potential $v_{\mathrm{eff}}\left(\boldsymbol{r}\right)$, which is given by the functional derivative

$$v_{\mathrm{eff}}\left(\boldsymbol{r}\right) = \frac{\delta}{\delta n}\left(V + U_{\mathrm{H}} + E_{\mathrm{XC}}\right) = v_{\mathrm{ext}}\left(\boldsymbol{r}\right) + \int \frac{n\left(\boldsymbol{r'}\right)}{\left|\boldsymbol{r}-\boldsymbol{r'}\right|}\mathrm{d}^3\boldsymbol{r'} + \frac{\delta E_{\mathrm{XC}}}{\delta n}. \tag{11}$$

Similar to the Hartree–Fock method, these equations can be solved iteratively with an initial guess for either the electron density n or the KS orbitals ϕ_i. When these self-consistent field iterations converge, the system's total energy is given by [21]

$$E^{\mathrm{tot}} = \sum_{i}^{N_{\mathrm{el}}} \epsilon_i - U_{\mathrm{H}}[n_0] + E_{\mathrm{XC}}[n_0] - \int \left.\frac{\delta E_{\mathrm{XC}}}{\delta n}\right|_{n_0} n_0(\boldsymbol{r})\mathrm{d}^3\boldsymbol{r} \ . \tag{12}$$

It should be noted that the KS orbitals for themselves do not have a strict physical meaning, they just represent a fictitious system of non-interacting electrons, which produce the same electron density as the real system. However, it is a common practice to interpret the KS eigenenergies ϵ_i as electronic density of states and derive bandgaps with them. Although the KS system is not intended to represent any quantity beside the electron density, this approach works very well. A rigorous proof which justifies this practice is to the best of our knowledge still missing.

2.4 Exchange-Correlation Functionals and Pseudopotentials

As already mentioned, the exact exchange-correlation functional E_{XC} is unknown and is probably so complex that it would be of no use in practical DFT calculations. To overcome this, several different approximations for E_{XC} have been proposed. These approximations are often fitted to well-known experimental data in order to give accurate values for specific physical quantities of interest. Strictly speaking, DFT is not entirely an ab-initio method, but rather bridges the gap between purely empirical classical force-field methods and accurate, but extremely expensive wavefunction based ab-initio approaches. Therefore an important part of DFT simulations is the selection of a XC functional, which is well suited for the system at hand or at least to chemically similar systems.

The first and simplest XC approximation assumes a homogenous electron gas and was proposed by Kohn and Hohenberg in their seminal work [20]. In this so-called local density approximation (LDA) the XC functional is determined only by the local electron density and can be expressed as

$$E_{\mathrm{XC}}^{\mathrm{LDA}} = \int n\left(\boldsymbol{r}\right) \epsilon_{\mathrm{XC}}\left(n\right) \mathrm{d}^3\boldsymbol{r}. \tag{13}$$

The function ϵ_{XC} is very well known from the Thomas–Fermi model [23] and quantum mechanical Monte Carlo simulations [24]. Although the LDA can give surprisingly good results in molecules, it generally overestimates binding energies and is not suitable for solids [25]. Furthermore, this approximation naturally fails for strongly localized charges with rapid variations of the electron density, which is highly relevant for the study of charged defects.

The main problem with LDA is its local dependency on the electron density, whereas the exact functional has to be a non-local property. To overcome this, the so-called semi-local or generalized gradient approximations (GGA) were introduced. These functionals include the density gradient and are of the form

$$E_{\mathrm{XC}}^{\mathrm{GGA}} = \int n\left(\boldsymbol{r}\right) \epsilon_{\mathrm{XC}}^{\mathrm{GGA}}\left(n, \nabla n\right) \mathrm{d}^3\boldsymbol{r}. \tag{14}$$

Many different GGA functionals were proposed in the literature, among the most popular ones are the PBE [26] and PW91 [27] functionals. These functionals often provide better results than LDA when applied to suitable systems [28].

LDA and GGA can give reasonable results for geometries and activation energies; however, they consistently underestimate the electronic bandgap. This phenomenon is known as the infamous DFT-bandgap problem. For the study of charge transfer in oxide defects, the position of the charge trapping level with respect to the band edges is of utmost importance. Therefore these methods are inadequate for the simulation of defects with DFT. In order to solve the bandgap-problem, the so-called hybrid functionals have been developed. They are based on GGA functionals, but mix in a portion of the exact two-electron non-local exchange energy from the HF method [29]

$$E_{\mathrm{X}}^{\mathrm{HF}}[n] = -\sum_{i>j} \iint \frac{\phi_i^*(\boldsymbol{r})\,\phi_j^*(\boldsymbol{r}')\,\phi_j(\boldsymbol{r})\,\phi_i(\boldsymbol{r}')}{|\boldsymbol{r}-\boldsymbol{r}'|} \mathrm{d}^3\boldsymbol{r}\,\mathrm{d}^3\boldsymbol{r}'. \tag{15}$$

Using hybrid functionals allows an accurate prediction of the electronic bandgap, commonly within 10% of the experimental value [30]. Most DFT studies on defects therefore use hybrid functionals in order to predict trap levels accurately. The most frequently used hybrid functionals are HSE [31], PBE0 [32], and B3LYP [33]. Most results reviewed in this chapter were obtained with a variant of the PBE0 functional. It should be kept in mind that hybrid functionals are far more computationally expensive than simple LDA or GGA schemes. Due to the four-center integral in Eq. 15 the computational costs scale with $\mathcal{O}(N^4)$ and therefore become a limiting factor in the feasible structure size. The detrimental scaling can be mitigated by using certain approximation schemes like the Auxiliary Density Matrix Method (ADMM) [34], which can calculate the HF exchange accurately on a reduced basis set.

The computational cost of any DFT calculation obviously depends on the number of electrons in the system. Furthermore, the wavefunctions of the inner electrons are rapidly oscillating in space due to their high energy. A quantum mechanical description of all electrons in the system would therefore need a very large basis set in order to accurately treat electrons in the vicinity of the core. The use of such large basis sets requires a lot of computational effort and is often even unfeasible for large systems. In order to keep computational costs low, the so-called frozen-core approximation is frequently employed. In this approximation only valence electrons are treated within DFT, whereas the effect of the core electrons is reduced to a screened Coulomb potential for the atomic core, the so-called pseudopotential. This approach is justified, since core electrons hardly ever engage in chemical bonding. The pseudopotential is created by optimizating parameters of an analytical potential against the results of an all-electron calculation for each chemical element of interest. It should be noted that this procedure already employs a certain XC functional for the all-electron calculations; therefore, pseudopotentials are linked to the functional being used for its creation.

3 Modeling of Amorphous Structures

For the study of oxide defects a suitable model for the host oxide is needed. In essence, there are two different approaches for modeling the oxide surrounding the defect. From a chemical perspective, a small cluster of the host material inside a closed simulation cell can be used to study defects. In order to increase the accuracy of this rather crude model, the isolated cluster can be embedded in a potential, which mimics the impact of the surrounding host material. This is known as the embedded cluster approximation (ECA) [35]. A more physical approach uses a model containing a few hundred atoms of the host material and enforces periodic boundary conditions on the system in order to mimic an extended bulk material [36]. Both of these methods were improved over the years and can provide accurate descriptions of point defects. However, since all results presented in this work are obtained with periodic models of amorphous materials, in the following we will only focus on this method. A description of defect modeling within the embedded cluster method can be found in [37].

3.1 Melt-Quench Technique

Periodic boundary conditions are widely used in solid-state physics to describe crystals and their band structures. Theoretical modeling of defects in crystalline materials is a rich field, which provides valuable insights into many phenomena like doping, diffusion processes, or the performance of electronic devices. In fact, the first theoretical studies on oxide defects were conducted in crystals like α-quartz [38]. However, deposited gate oxides are generally amorphous. In the context of device reliability the modeling of oxide defects therefore requires knowledge about the distribution of defect parameters within the amorphous gate oxide. Furthermore it has been demonstrated that some defects occurring in a-SiO_2 like the hydroxyl-E$'$ center are not stable in α-quartz [39] and therefore cannot be studied in crystalline models. To obtain a more complete picture, it is thus required to also study defects in amorphous model structures.

The most popular approach to create amorphous model structures simulates the melting of a crystal within a periodic cell, followed by an equilibration of the melt at high temperatures and a rapid cooling afterwards. This physically motivated technique is called melt-quench method and is illustrated in Fig. 2. Hereby the melting and cooling of the material is simulated using molecular dynamics (MD) [36]. In MD simulations the temporal evolution of a system is studied within the framework of classical mechanics, where particles move in an interatomic force field according to Newton's laws of motion. However, the study of the system behavior at varying temperatures or pressures within MD requires the ability to control these thermodynamic quantities. This is usually achieved by extending the equations of motion with terms which enforce, e.g., the

Fig. 2 Initial crystalline SiO_2 and final a-SiO_2 structure of a melt-quench run. The yellow and red spheres indicate Si and O atoms, respectively. The initial configuration is a $2 \times 2 \times 2$ supercell of β-cristobalite, a high-temperature crystalline polymorph of SiO_2, containing 216 atoms. This crystal is an ideal starting point, since it has a cubic lattice and its density of 2.33 g/cm^3 is close to the experimental value of 2.2 g/cm^3 for a-SiO_2. The crystal was melted at 5000 K for 1 ns and afterwards cooled with a rate of 6 K/ps. Note that the volume of the simulation cell is allowed to change during this process [36]

temperature (thermostat) or the pressure (barostat). More information regarding MD and different thermostat and barostat models can be found in [40]. The simulation of melt and quench processes typically has to cover a time span of several nanoseconds to allow the structure to properly equilibrate. Due to the large amount of energy and atomic force evaluations needed, DFT is rarely used during these steps. Instead, the MD simulation is performed with classical interatomic force fields. The geometry and cell parameters of the resulting amorphous structures are then further optimized with DFT to reduce internal stress and to obtain a proper electronic structure. The used force field must be parameterized carefully and must be able to describe chemical reactions of the involved chemical elements in order to produce physically meaningful structures. For example, a-SiO_2 structures can be created with the ReaxFF [41] force field, a suitable force field for a-HfO_2 is presented in [42].

It should be mentioned at this point that often highly unphysical parameters are needed for a melt-quench run. For example, the creation of amorphous SiO_2 structures requires temperatures of up to 5000 K. The high temperature can be ascribed to the use of empirical force fields, the absence of nucleation centers as well as the confinement of the system inside the simulation cell. Also an extremely high cooling rate of up to 6 K/ps is used to significantly reduce the number of needed simulation timesteps [36].

3.2 Structural Verification

The internal structure of amorphous materials strongly depends on the involved manufacturing processes as well as preparation conditions like temperature and pressure. For example, the structure can be partially crystallized due to annealing.

This ambiguity makes modeling of amorphous materials for a specific application particularly hard. For that reason, the structures obtained from the melt-quench technique should be compared to available experimental data of the material system in question. Basic structural tests can include comparisons to the experimental density and electronic structure. Furthermore, the spatial behavior of the band edges across the structures should be checked with an analysis of the local density of states. This is necessary to detect spurious electric fields, which lead to artificial band bending. More details on structural verification can be found in [36]. In the following we briefly discuss two powerful structural model tests from experimental data.

Particularly useful information about the internal structure of amorphous solids can be gained from the structure factor $S(Q)$ obtained from X-ray or neutron diffraction measurements. For isotropic materials the structure factor can be written as [43]

$$S(Q) = \frac{1}{N} \sum_{i,k} f_i f_k \frac{\sin(Q\,|\boldsymbol{R}_i - \boldsymbol{R}_k|)}{Q\,|\boldsymbol{R}_i - \boldsymbol{R}_k|}. \tag{16}$$

Here, f_i and f_k are the atomic form factors, describing the scattering amplitudes of the involved atoms. Q is the amplitude of the scattering vector and R_i,R_k are the atomic positions. The structure factor can be obtained from experiment but is also easily accessible from the amorphous model structures. A comparison of $S(Q)$ between experiment and atomistic model structures for a-SiO_2 is given in Fig. 3. As can be seen, these models are in good agreement with experimental data, indicating the validity of the melt-quench method and the used force fields.

Another way to test model structures is offered by infrared absorption and Raman scattering experiments. In these measurements incoming photons from an IR laser couple inelastically to vibrational states of the target material. The resulting spectra are therefore linked to the vibrational density of states (VDOS) in the

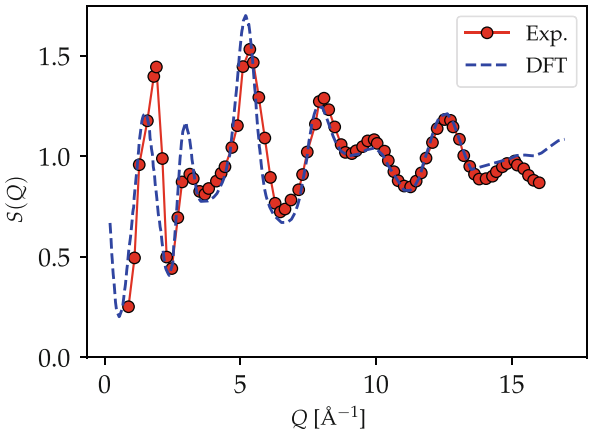

Fig. 3 Comparison of structure factors between experiments [44] and DFT optimized a-SiO_2 models obtained from the melt-quench procedure using the ReaxFF force field. The model structures show good agreement with the experimental data. The match of signal peak positions for large Q values indicate a proper long-range order of the used models. Modified from [36]

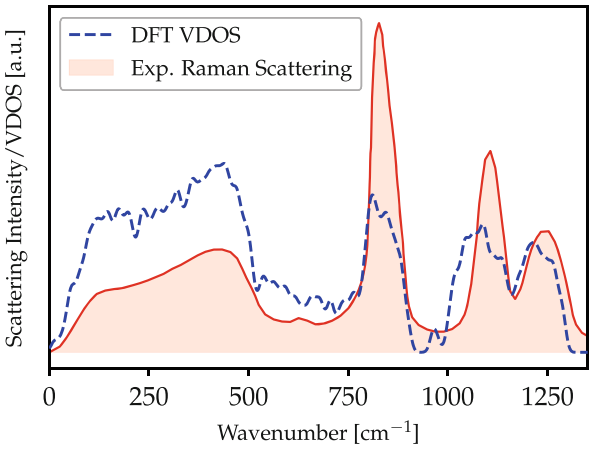

Fig. 4 Comparison between experimental Raman scattering intensities [46] and the vibrational density of states (VDOS) in an a-SiO_2 model obtained from DFT calculations. As can be seen, the positions of the signal peaks match well between DFT and experiment

target. Since the VDOS of a structure can be predicted with DFT calculations, such measurements can be used to compare model structures to real systems. Within the harmonic approximation the phonon modes of the structure can be derived from the force constant matrix, which is defined by

$$\Phi_{jk} = \frac{1}{\sqrt{M_j M_k}} \left. \frac{\partial^2 E^{\text{tot}}}{\partial R_j \partial R_k} \right|_{\tilde{\boldsymbol{R}}=\tilde{\boldsymbol{R}}_0} = \frac{1}{\sqrt{M_j M_k}} \left. \frac{\partial F_k}{\partial R_j} \right|_{\tilde{\boldsymbol{R}}=\tilde{\boldsymbol{R}}_0} . \tag{17}$$

Here M_j is the mass of the j-th ion. The force constant matrix essentially describes the curvature of the potential energy surface $E^{\text{tot}}(\tilde{\boldsymbol{R}})$ at the minimum configuration $\tilde{\boldsymbol{R}}_0$. By definition this matrix is positive-definite and its eigenvalues ω_j^2 are the squared classical vibrational frequencies of the structure [45]. Figure 4 shows the resulting phonon density of states alongside experimental Raman scattering intensities for the used a-SiO_2 models. There is good agreement on the peak positions between the experimental data and the results obtained from DFT. This finding is another piece of evidence for the validity of the used structural models. It should be noted that within this simplified classical model only peak positions are predicted correctly. The simulation of complete Raman and IR absorption spectra from ab-initio methods is more involved and requires the consideration of quantum mechanical selection rules. For more details we refer the interested reader to the literature [47].

3.3 Interface Models

In order to describe the charge transfer between oxide defects and device substrate, an atomistic model of the oxide/channel interface as depicted in Fig. 5 is needed. Such interface structures can be created using a modification of the melt-quench

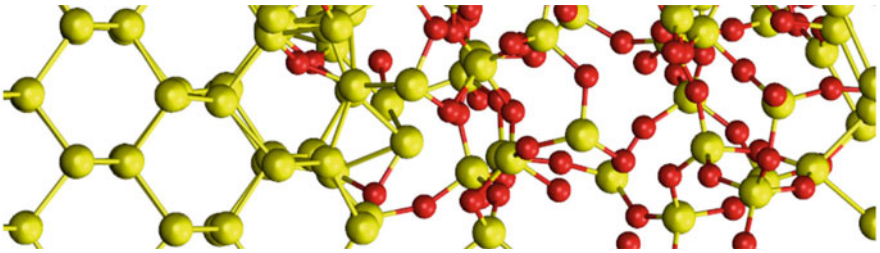

Fig. 5 Atomistic model for an interface between crystalline Si (left) and a-SiO_2 (right) [36]

method, as is outlined in [36]. However, obtaining an accurate interface model is far more difficult than simple bulk oxide models due to the limited experimental knowledge of the transition region between oxide and substrate. When analyzing charged defects in those structures with DFT another problem arises. Simply adding electrons or holes to the system does not guarantee a charge localization at the oxide defect. Since DFT determines the electronic ground state by minimizing the energy functional, additional charges may simply be delocalized in the substrate valence or conduction band if energetically favorable. Although charges can be forced into certain regions of the simulation cell with constrained DFT (CDFT) [48], such calculations are very expensive and thus rarely found in literature. In fact, all results presented in this work are obtained from bulk oxide models. In these bulk models the charge transfer between oxide defect and the substrate valence or conduction band is not accessible within DFT. This has some implications on the modeling of charge transitions as will be outlined in Sect. 4.3.

3.4 Formation Energies and Thermodynamic Trap Levels

The valence and conduction band of the substrate act as charge reservoirs for the oxide defects. Since the substrate is not included in the DFT models, the energy of charge carriers in these reservoirs must be included explicitly in the DFT energies of the different defect charge states. The standard approach to account for the carrier energy in the reservoir is to compare the so-called formation energies of the different defect states

$$E_{\mathrm{Q}}^{\mathrm{f}}(\tilde{\boldsymbol{R}}) = E_{\mathrm{Q}}^{\mathrm{tot}}(\tilde{\boldsymbol{R}}) - E_{\mathrm{bulk}}^{\mathrm{tot}} - \sum_i \mu_i n_i + q E_{\mathrm{F}} + E^{\mathrm{cor}}. \tag{18}$$

Here $E_{\mathrm{Q}}^{\mathrm{f}}$ denotes the formation energy of the defect state with a net charge

$$Q \in \{\ldots, -1, 0, +1, \ldots\},$$

the total DFT energy of this state is termed $E_{\mathrm{Q}}^{\mathrm{tot}}$ and $E_{\mathrm{bulk}}^{\mathrm{tot}}$ is the total energy of the defect-free neutral bulk oxide. The terms $\mu_i n_i$ account for the chemical energy needed to add or remove certain atoms to create the defect from a pristine bulk. Since all defects studied in this work are composed of the same atoms in every charge state, this term is just a constant energy offset and can be omitted. Contributions due to the chemical potential are only important if total formation energies are needed, e.g., to estimate the defect concentration. E_{F} denotes the Fermi level of the charge reservoir and is usually referenced to the valence band edge of the oxide

$$E_{\mathrm{F}} = E_{\mathrm{VBM}} + \epsilon_{\mathrm{F}}. \tag{19}$$

E_{VBM} is the energy of the valence band maximum of the oxide. It can be approximated by the energy of the highest occupied KS-orbital obtained by an electronic density of states analysis of the bulk system [49].

When dealing with charged defects in a periodic cell, the electrostatic potential within the cell would be infinite due to the slowly decaying Coulomb contributions of all other repeated cells. To avoid this problem, a net charge within the periodic cell is compensated by a fictional background charge of opposite sign to keep the cell potential finite. Although this approach leads to a bounded electrostatic potential, it introduces an unwanted interaction between the defect charge and the neutralizing background charge. Furthermore, there is also a spurious electrostatic interaction between the charged defect and its periodic images. Especially for small simulation cells this interaction must be balanced out by a charge correction term E^{cor}. Several methods for this charge correction have been proposed, among the most popular schemes are the Lany–Zunger [50] and the Freysoldt–Neugebauer–Van de Walle [51] corrections. An excellent review of the different charge correction schemes for defects in bulk materials can be found in [52].

The defect formation energy is an important quantity to evaluate the thermodynamical stability of the different defect states. As can be seen in Fig. 6, a certain

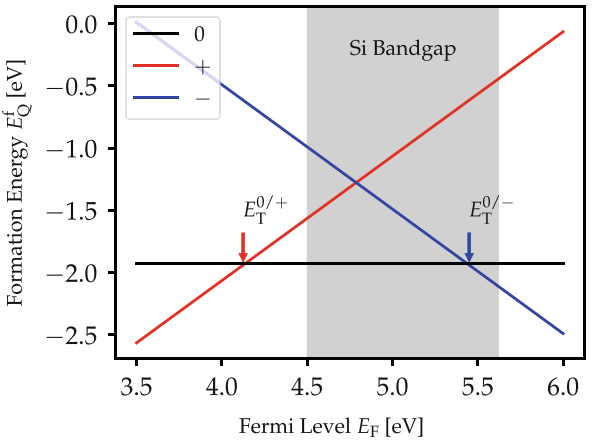

Fig. 6 Formation energies of a hydrogen bridge defect in a-SiO_2 in different charge states. The Fermi level is given with respect to the SiO_2 valence band. The shaded region indicates the bandgap of the Si substrate. The charge trapping levels are given by the Fermi levels at which two formation energies cross. These points are easily detectable in experiments. Modified from [53]

charge state is only stable in a certain range of the Fermi level. The boundary between two such regions is called the charge trapping level (CTL). When the Fermi level matches the charge trapping level, the corresponding defect states are equally stable, which leads to a 50% occupancy in equilibrium and therefore results in maximal power of the RTN signal. Thus the CTL is easily accessible in experiments by varying the gate bias voltage [6] and is an important parameter for comparing defect candidates in DFT to experimental data. In the case of defects in SiO_2 and HfO_2 such comparisons are given in Sect. 5.4 and Sect. 6.3, respectively.

4 The Four-State NMP Model

The discovery of degradation mechanisms like BTI and RTN sparked the development of several models to describe these phenomena. Earlier models were based on a classical reaction-diffusion process involving atomic hydrogen [54, 55]. These models were widely accepted in industrial applications. However, new experimental findings obtained from techniques like TDDS are incompatible with these models [56]. Modern modeling attempts focus on reaction-limited processes involving state changes of defects in the oxide or at the interface. Early oxide defect models were derived from the famous Shockley–Reed–Hall (SRH) model [57, 58], which was originally derived for defects in the device channel. The SRH model was extended in order to account for the tunneling of charges to the oxide [59] and transition barriers for the experimentally observed temperature-activated charge transfer [1]. Although these adapted models must be considered as milestones in reliability physics, they were lacking a solid physical foundation. In this section, we briefly recap the fundamentals of the 4-state nonradiative multiphonon model [6, 60–62], which is capable of accurately describing BTI and RTN in a unified framework. This model treats the charge transfer reactions between defects and device substrate within the nonradiative multiphonon theory (NMP) [63, 64]. An in-depth discussion on the 4-state NMP model can be found in [65].

4.1 Experimental Evidence for the Four-State NMP Model

Electrical defect characterizing methods like the temporal analysis of RTN signals or TDDS can be used to extract statistics of the time constants for charge transfers in the devices. Furthermore, the temperature and bias dependency of these time constants can be measured. A detailed description of experimental parameter extraction is given in Chapter 7 of this book [10]. The following key experimental findings lead to the development of the 4-state NMP model [65, 66]:

- As shown in Fig. 7 the characteristic time constants for charge capture and emission, denoted by τ_c and τ_e, respectively, are very sensitive to temperature.

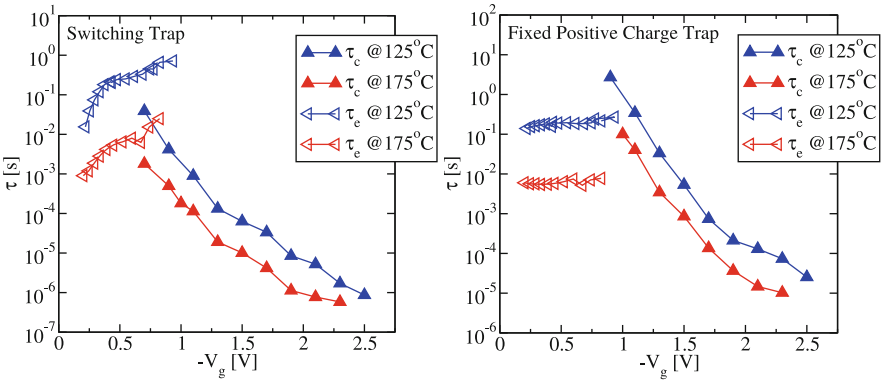

Fig. 7 Experimental capture and emission time constants of two different defects obtained through TDDS measurements. τ_c and τ_e strongly decrease with higher temperatures. **Left:** For a switching trap, both charge capture and emission depend exponentially on the applied gate bias. **Right:** In contrast, τ_e is nearly bias-independent for a so-called fixed charge trap. Adapted from [67]

This indicates a thermally activated process being involved in charge transfer reactions between the oxide and the substrate. The mean time constants can be expressed as

$$\tau_i \propto \exp\left(\frac{E_{\mathrm{A},i}}{k_{\mathrm{B}}T}\right) \tag{20}$$

according to Arrhenius's law with an activation energy $E_{\mathrm{A},i}$. This finding rules out a SRH-like mechanism for charge trapping in oxide defects. However, charge transfer based on NMP theory is consistent with these results.

- The charge capture times depend exponentially on the applied gate bias V_{G}, which can be easily explained for a NMP process as will be demonstrated in Sect. 4.3. Furthermore, defects can be categorized in fixed traps and switching traps depending on the bias-sensitivity of the emission times, see Fig. 7 (left) and (right), respectively. In the case of fixed traps, the emission time is nearly independent of the bias. This indicates the existence of metastable states, which allow different competing reaction paths.
- It was demonstrated that a high-frequency bias significantly increases the resulting capture times. This finding can also be explained with additional defect states, which limit the overall transition rates.

Most of these experimental findings were obtained for hole traps responsible for NBTI in SiO_2 based devices. However, recent results suggest a similar behavior for electron traps in high-κ materials like HfO_2. Therefore, it can be assumed that the 4-state model is also applicable to electron traps in these materials as well [68, 69].

4.2 State Diagram

Within the 4-state model defects are treated as Markov chains with two stable states (1, 2) and two metastable states (1′, 2′). Using Markov chains for the description implicitly assumes the defect to be memory-less. This means, the defect behavior is solely determined by its current state but not the entire history of the defect. This assumption is crucial for modeling and is justified by the extremely fast relaxation into the new configuration after a transition [70]. The resulting state diagram is depicted in Fig. 8. The states 1 and 1′ represent electrically neutral defect configurations, whereas 2 and 2′ are charged states with either an electron or hole trapped at the defect site. In this model, a shift in the threshold voltage can only be observed when the defect changes its charge state, i.e., during the transitions $1 \Leftrightarrow 2'$ and $2 \Leftrightarrow 1'$. The thermal transitions $1 \Leftrightarrow 1'$ and $2 \Leftrightarrow 2'$ account for possible structural relaxation of the defect without charge transfer. Such transitions are not directly detectable with electrical measurements, since they do not change the device electrostatics. However, the experimentally observed decorrelation of τ_c and τ_e as well as the occurrence of fixed traps are clear evidence for their existence [71].

4.3 Transition Rates

The abstract description in the 4-state model with Markov chains is completely agnostic towards the microscopic nature of the defect. However, the parameters within the model allow the calculation of the macroscopic defect behavior, in partic-

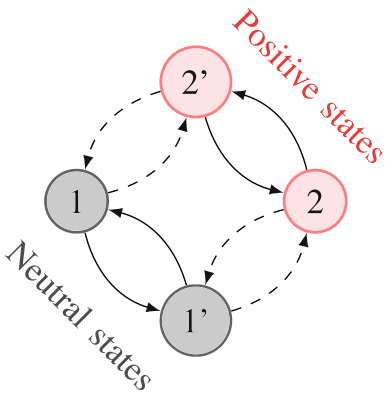

Fig. 8 The 4-State model for oxide defects. The defect is assumed to exist in a stable and metastable configuration both in the neutral and charged state. Here, the metastable states are indicated with a prime. Thermal transitions are represented by solid lines between states with the same charge, whereas NMP charge transitions are drawn as dashed lines between states with different charges

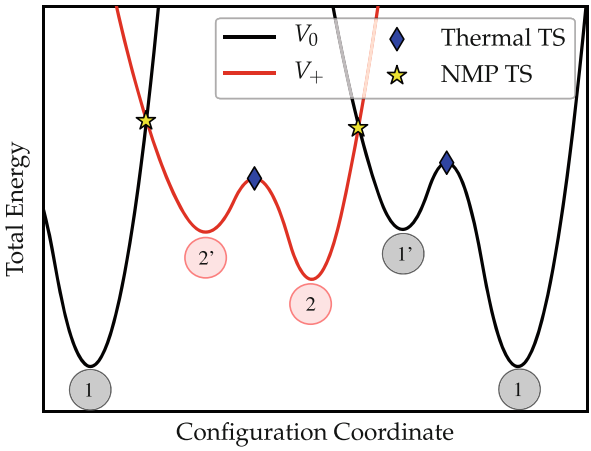

Fig. 9 Schematic energy profiles between the different states of the 4-state model. In this picture the states are given by the minima of the energy profiles. The transition rate for thermal transitions is determined by the point with highest energy along the reaction path. In the classical limit of NMP theory charge transitions occur at the intersection points of the surfaces. Modified from [72]

ular τ_c and τ_e as a function of the gate voltage V_G, from a solid physical foundation and are therefore also accessible through experiments. The model parameters can be also extracted from DFT calculations, which allows the identification of suitable defect candidates to describe the measurement data.

In the 4-state model all physics is condensed into the transition rates k_{ij} from an initial state i to a final state j. Since these transitions are temperature-activated, a certain energy barrier E_{ij} has to be overcome. The barriers in the 4-state model can be depicted with potential energy profiles as shown in Fig. 9. In these plots the electronic potential energy surfaces $V_i(\tilde{\boldsymbol{R}})$ are evaluated along a path between the initial and final state, resulting in energy profiles $V_i(q)$ as a function of the so-called configuration coordinate q. Using this picture, the defect states lie in minimum configurations of the potential energy surfaces. In the case of the thermal transitions $1 \Leftrightarrow 1'$ and $2 \Leftrightarrow 2'$ the transition barrier is determined by the classical transition state (TS), whereas the transition state of the NMP transitions is in a classical picture given by the intersection point between the corresponding potential energy surfaces. In the following we will discuss how the resulting barriers are linked to transition rates and how they can be determined from DFT simulations.

Thermal Transitions

In thermal transitions there is no charge transfer between the defect and the device substrate. Thus the defect is described by the same potential energy surface throughout the transition. Assuming a classical movement of the nuclei on the energy surface, the mean thermal transition rates can be determined within classical transition state theory [73, 74] and are given by

$$\tau_{ij}^{-1} = k_{ij} = \nu_0 \exp\left(-\frac{E_{ij}}{k_B T}\right). \tag{21}$$

Here E_{ij} is the thermal barrier, which is determined by the transition state along the reaction path. ν_0 is known as the attempt frequency and is related to the vibrational frequency within the harmonic approximation. In most systems, a value of $\nu_0 = k_B T/h \approx 10^{13}$ Hz can be assumed for the attempt frequency [65].

In order to calculate the transition barrier E_{ij} for a specific defect in DFT, finding the TS between the two states on the high-dimensional potential energy surface is required. Finding a transition state is more involved than the determination of minimum states, which can be easily found with various optimization schemes [75]. The standard approach for finding transition states in DFT relies on the nudged elastic band (NEB) method [76]. This method uses a band of intermediate configurations, which connects the two states of interest. The total energy of the whole band is then minimized, driving the intermediate configurations towards the minimum energy path between the states. The TS is then given by the configuration with highest energy along this path.

Nonradiative Multiphonon Transitions

Contrary to thermal transitions, NMP transitions describe the transfer of charges. This involves a change of the electronic state and thus a crossing between potential energy surfaces as shown in Fig. 10. In this case, the transition is governed by Fermi's Golden Rule in combination with the Franck-Condon principle [78, 79]. The resulting transition rate can be expressed as [65]

$$k_{ij} = A_{ij} f_{ij} , \tag{22}$$

where A_{ij} is the electronic matrix element and f_{ij} is the so-called lineshape function.

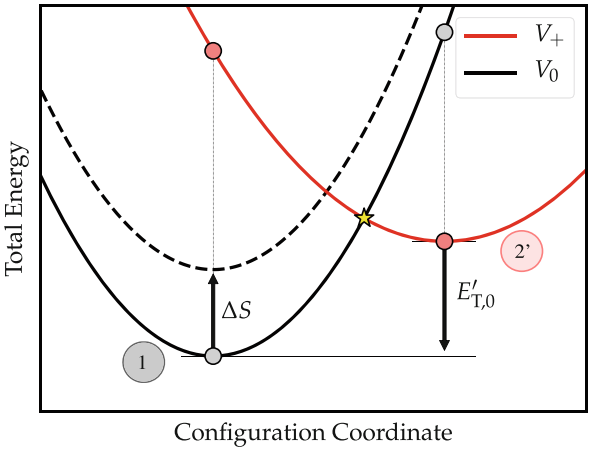

Fig. 10 NMP transition within the harmonic approximation. Here the energy profiles are approximated by parabolas. The small circles indicate the DFT energies, which are used to calculate the harmonic approximation. An applied gate bias shifts the energy profiles relative to each other by ΔS. This leads to bias dependent intersection points (IP) and transition barriers. Adapted from [77]

The electronic matrix element, which describes the coupling between the defect states and the device substrate, is given by

$$A_{ij} = \frac{2\pi}{\hbar} \left| \langle \psi_i | \hat{H}' | \psi_j \rangle \right|^2 \tag{23}$$

with the perturbation operator $\hat{H}'$. A_{ij} is not obtainable from bulk oxide DFT simulations since information about the wavefunctions of the charge reservoirs in the substrate valence and conduction band is not available. Instead, A_{ij} is frequently approximated by a semi-classical approach

$$A_{ij} \approx v_{\text{th}} \sigma \vartheta. \tag{24}$$

Here $v_{\text{th}} = \sqrt{8 k_{\text{B}} T / \pi m^*}$ denotes the thermal velocity of the charge carriers in the substrate, σ is an effective capture cross section, which is fitted to experimental data (e.g., $\sigma = 3.0 \times 10^{-14}\,\text{cm}^2$ [80]). ϑ is a tunneling factor given by

$$\vartheta = \exp\left(-\frac{x_{\text{t}}}{x_0} \right), \tag{25}$$

where x_0 is an effective tunneling length from a WKB approximation [81] and x_{t} is the distance of the defect from the interface.

The lineshape function f_{ij} accounts for the vibrational overlaps between the two states. Assuming a thermal equilibrium in the initial state, the lineshape function can be written as

$$f_{ij} = \underset{\alpha}{\text{ave}} \left(\langle \eta_{i\alpha} | \eta_{j\beta} \rangle \, \delta \left(E_{i\alpha} - E_{i\beta} \right) \right). \tag{26}$$

Here ave stands for the thermal average within a canonical ensemble. However, implementations of the NMP model in device simulators typically use a much simpler approach for the lineshape function. In the limit of high temperatures it can be shown [62] that the lineshape function is only determined by the classical intersection point of the corresponding potential energy surfaces

$$f_{ij} \approx \exp\left(-\frac{E_{ij}}{k_{\text{B}} T} \right). \tag{27}$$

Here, E_{ij} denotes the classical barrier defined by the intersection point. However, a similar problem arises here as for the thermal transitions discussed earlier. Due to the exponential dependence on the barrier height, the reaction path with the lowest possible barrier dominantly contributes to f_{ij}. Although this minimum energy path can be found in DFT by applying constraint optimization algorithms [82], such methods are rather expensive for the study of oxide defects, especially when dealing with an ensemble of defects as is the case in amorphous oxides. Instead, the potential energy surfaces are approximated by parabolas as indicated in Fig. 10. Within this

approximation the energy profiles are solely determined by a fit to the energies of four DFT single-point calculations. The resulting parabolas are then used to calculate the intersection point and the classical lineshape function f_{ij}.

One important aspect, which has to be considered, is that the formation energies of the defect are influenced by the applied gate bias. On the one hand this influence is introduced by the change of the Fermi level within the charge reservoirs. On the other hand the difference in electrostatic potential between defect and device channel results in an additional energy shift. This effect is accounted for by a field-dependent trap level. Assuming a charge-free dielectric, a simple linear model for the trap can be used

$$E_\mathrm{T} = E_{\mathrm{T},0} + \Delta S \quad \text{with} \quad \Delta S = QFx_\mathrm{t}. \tag{28}$$

Here, $E_{\mathrm{T},0}$ is the trap level at flatband conditions and F is the electric field inside the oxide. Furthermore, oxide defects can potentially exchange charges with many states within the semiconductor valence or conduction band. The total transition rate is therefore given by a summation over all band states. For example in the case of hole traps this results in the transition rates

$$k_{12'} = \int_{-\infty}^{\infty} D(E) f_p(E) A_{12'}(E, E_\mathrm{T}) f_{12'}(E, E_\mathrm{T}) \mathrm{d}E \tag{29a}$$

$$k_{2'1} = \int_{-\infty}^{\infty} D(E) f_n(E) A_{2'1}(E, E_\mathrm{T}) f_{2'1}(E, E_\mathrm{T}) \mathrm{d}E. \tag{29b}$$

Here D is the substrate's density of states, f_n and f_p are the occupation probabilities for electrons and holes, respectively. Note that the matrix element A_{ij} as well as the lineshape function f_{ij} are expressed as a function of the trap level E_T and the energy E of the charge reservoir state. Applied to a pMOS device and given the additional assumption that defects mostly interact with the Si valence band edge, Eq. 29 leads to a simple analytical expressions for the transitions rates:

$$k_{12'} = p v_\mathrm{th} \sigma \vartheta \exp\left(-\frac{E_{12'}}{k_\mathrm{B} T}\right) \tag{30a}$$

$$k_{2'1} = p v_\mathrm{th} \sigma \vartheta \exp\left(-\frac{E_{2'1} + E_{\mathrm{V,Si}} - E_\mathrm{F}}{k_\mathrm{B} T}\right). \tag{30b}$$

The resulting NMP transition rates reflect the experimental findings. Firstly, charge transitions depend exponentially on the gate bias, which changes the barriers $E_{12'}$ and $E_{2'1}$. Furthermore, the NMP rates explain the observed thermal activation. From Eq. 29 or 30 one can extract activation energies for defect candidates with DFT, which also allows a comparison to experimental data.

In our derivations we mainly focused on hole traps and their interaction with the substrate's valence band; however, similar equations for transition rates can also be derived for electron traps. The full set of rate equations alongside an in-depth discussion of the NMP model can be found in [65].

5 Defects in Amorphous SiO_2

SiO_2 is the native oxide of the Si substrate and has therefore been used as gate dielectric since the early days of microelectronics. Although SiO_2 is increasingly replaced by high-κ materials like HfO_2 in order to improve the electrostatic channel control, the study of defects in a-SiO_2 is still highly relevant for reliability concerns. Defects in SiO_2 also play a role in modern high-κ gate stack structures since a thin SiO_2 layer always forms at the Si interface during oxide deposition. Defects in this layer can potentially trap charges rather easily due to the small distance to the channel and therefore contribute considerably to BTI and RTN in high-k devices. Modern devices also use nitrided SiO_2 (SiON) in order to decrease the gate leakage current. As was shown experimentally in [83], defects in SiON behave similarly to the ones in pure SiO_2; therefore, it is sufficient to model defects in the much simpler SiO_2 system. The Si/SiO_2 material system is well understood both experimentally and theoretically; a plethora of data is therefore available as a reference for theoretical defect studies using DFT. Furthermore, defect densities can be kept low in the Si oxidation process, which allows an experimental characterization of individual defects in small-area devices using techniques like TDDS. In the following, the key findings of recent ab-initio studies on defects in a-SiO_2 are summarized. All results presented here were obtained from periodic random network models containing 216 atoms, as described in Sect. 3.

5.1 Oxygen Vacancies

Presumably the most studied defect in silica is the oxygen vacancy [84–86]. It is formed when a two-coordinated O atom is missing from the a-SiO_2 network. This defect forms naturally during Si oxidation and the resulting defect concentration depends on processing parameters such as temperature and oxygen partial pressure [87]. Depending on the local defect environment, the oxygen vacancy can exist in various stable and metastable states with different charges [88]; it thus supports the aforementioned 4-state defect model, see Fig. 11. In the primary neutral configuration, the two Si atoms forming the vacancy bind together, which leads to long ranging distortions in the flexible a-SiO_2 network surrounding the defect.

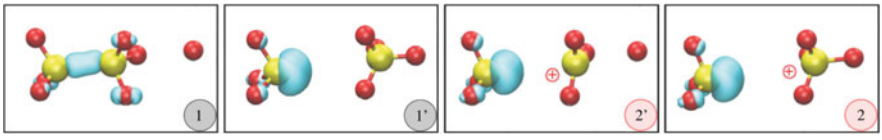

Fig. 11 Oxygen vacancy in a-SiO_2 with its different configurations mapped to the states in the 4-state model. The turquoise bubbles indicate the HOMO electron distribution [72]

Since all electrons in this configuration are paired, the state 1 of the OV does not carry a net spin and thus cannot be detected by spin-resonance measurements. If the vacancy traps a hole (State 2′), e.g., one of the electrons in the Si–Si bond is removed, the bond can break and the Si atoms move apart from each other, resulting in a Si dangling bond. In other cases, hole trapping only weakens the Si–Si bond instead of breaking it, the resulting spin density is then shared between the two Si atoms, which is known as the dimer configuration [88, 89]. In both cases, there is an unpaired electron, which is detectable in ESR measurements. It is assumed that these two configurations correspond to the experimentally observed E' center defect in a-SiO_2 [90]. In addition, the Si atom without a dangling bond can move through the plane spanned by its O neighbors. Depending on the local environment, the backprojected Si atom can be stabilized by a nearby O (see Fig. 11 state 1′ and 2). This process is termed puckering and is associated with a thermally activated transition without charge transfer, e.g., the transitions $1 \Leftrightarrow 1'$ and $2 \Leftrightarrow 2'$ in the 4-state model. The positive state 2 is believed to be the frequently measured E'_γ center [90].

Although the OV defect is in principle compatible with the 4-state model, multiple theoretical studies [72, 91, 92] clearly show that the hole trap level of this defect is too far below the silicon valence band edge ($E_T - E_{V,Si} \approx -3.5\,eV$). In order for the OV to trap a hole, thick oxides and large electric fields would be needed. However, in a modern pMOS device with a thin oxide layer the OV remains neutral under all relevant bias conditions and cannot contribute to NBTI or RTN through to hole trapping.

5.2 *Hydrogen-Induced Defects*

Although some models suggested oxygen vacancies as the cause of NBTI [93], the focus has recently shifted towards hydrogen-related oxide traps [14, 94]. During the forming gas anneal process, hydrogen is used to passivate Si dangling bonds at the Si/SiO_2 interface. This crucial step is necessary to reduce the high density of interface traps, which would otherwise occur and significantly degrade the device characteristics. However, experimental [95] as well as theoretical [96, 97] studies indicate that hydrogen easily diffuses in SiO_2 with activation energies as low as 0.2 eV. Furthermore it was shown that there is a connection between hydrogen concentration during anneal and the resulting density of electrically active oxide traps [14, 94]. DFT studies indicate that H can form promising candidates for active defects like the hydrogen bridge or the hydroxyl-E′ center, which will be discussed in the following.

Hydrogen Bridge

Although the oxygen vacancy itself stays neutral under typical bias conditions, it acts as a precursor site for another related defect, the hydrogen bridge (HB) [98]. The HB is formed by the reaction of atomic hydrogen with an OV. DFT studies in α-quartz conducted by Blöchl et al. showed that the HB defect might be responsible for stress-induced leakage current (SILC) in gate oxides [99]. The formation of a HB defect from an interstitial H atom and an OV is nearly barrierless, whereas the reverse reaction of H release from the HB has a thermal barrier of 2.8 eV on average [100]. These reaction kinetics in combination with the abundance of vacancies and H suggest that a significant amount of HB defects are formed.

The most stable neutral configuration of the HB defect is shown as state 1 in Fig. 12. Here the atomic H binds to only one of the Si atoms forming the vacancy, leaving the other one undercoordinated. The resulting ESR from this dangling bond was first identified by Nelson and Weeks [101]. The Si–H bond length is rather constant at 1.47 Å, whereas the weak interaction with the second Si atom is strongly dependent on the local environment of the defect, which results in a large spread of the corresponding Si–H distances [72, 100]. The HB can capture a hole resulting in a configuration depicted in Fig. 12 state 2′. Here the remaining 2 electrons are shared between the two Si and the H atom, resulting in a nearly symmetrical configuration. Similar to the aforementioned OV in a-SiO_2, the HB can undergo a puckering transition in both charge states, where one Si atom moves through the plane spanned by its O neighbors.

Hydroxyl-E′ Center

In amorphous SiO_2 the Si–O bond lengths and angles do not have well defined values, but are widely distributed. It was shown in [100] that sites with distorted, but otherwise intact, Si–O bonds can interact with atomic hydrogen resulting in new defects, which do not exist in crystalline SiO_2. One such defect, the so-called hydroxyl-E′ center (H-E′), arises from the interaction of H with strained Si–O bonds, which are significantly longer than the equilibrium bond length of 1.61 Å in α-quartz [39]. In this case, H is able to bind to the oxygen atom and break one of the two Si–O bonds, resulting in a hydroxyl group facing a Si dangling bond as depicted in Fig. 13 (state 1). Such a configuration is more stable than the interstitial H by 0.8 eV on average. Due to the significant amount of strained bonds in a-SiO_2 and its

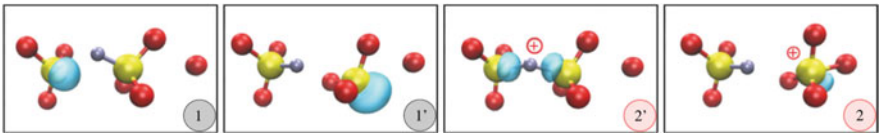

Fig. 12 Different configurations of the hydrogen bridge defect within the 4-state model [72]

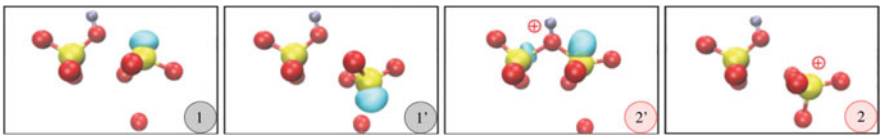

Fig. 13 Different configurations of the hydroxyl-E′ center within the 4-state model [72]

thermodynamical stability, the H-E′ center is expected to be formed in significant quantities, much larger than any other defect. By trapping a hole, the broken Si–O bond is restored and the positive H ion is bonded to the partially negative O atom by Coulomb interaction. The hydroxyl-E′ center also supports a 4-state defect model via a similar puckering transition as those of the OV and HB. Due to its thermodynamical trap levels (see Sect. 3.4) near the Si valence band, this defect is a promising candidate for explaining NBTI and RTN in pMOS devices [72].

In addition to the H-E′ center, another hydrogen-related defect in a-SiO_2 has been discovered recently [100]. H can donate its electron to a Si atom with a shortened bond (<1.6 Å) and binds electrostatically to the neighboring O atom. This results in a defect termed $[SiO_4/H]^0$ center where the Si–O–Si angle is stretched and an additional electron is localized at one of the Si atoms. Naturally, such a defect is formed more easily when H encounters a site with an already stretched Si–O–Si angle. It was shown that this defect is only slightly more stable (0.1–0.2 eV) than an interstitial H atom in a-SiO_2. Due to its lower thermodynamic stability and lower barriers for the H atom to become interstitial again compared to the H-E′ center, it was concluded that the interaction of H with the a-SiO_2 network primarily leads to H-E′ centers instead of $[SiO_4/H]^0$ centers.

5.3 Charge Trapping at Intrinsic Sites

Most atomistic studies on BTI and RTN are focused on charge trapping at defective sites of the host material. However, certain measured defect bands could not be linked to any known defects. One example of such an unidentified band are deep electron traps in SiO_2 with a trap level of 2.8 eV below the a-SiO_2 conduction band [102, 103], which are suspected to play a major role for PBTI in SiC based power devices. The observed high trap density of up to 5.0×10^{19} cm^{-3} in this defect band is not consistent with previous assumptions [104] that oxygen-deficient defects like the E′ center are responsible for these electron traps.

Based on these findings it was suggested that electron trapping does not only occur at defects but can happen spontaneously at certain sites in a-SiO_2. A recent theoretical study [105] found that the LUMO of the used a-SiO_2 models is partially localized at particularly long Si–O bonds, as depicted in Fig. 14 (left). Upon electron capture, this electronic state is filled and causes a pronounced structural distortion, which leads to the additional electron being localized at one particular Si atom

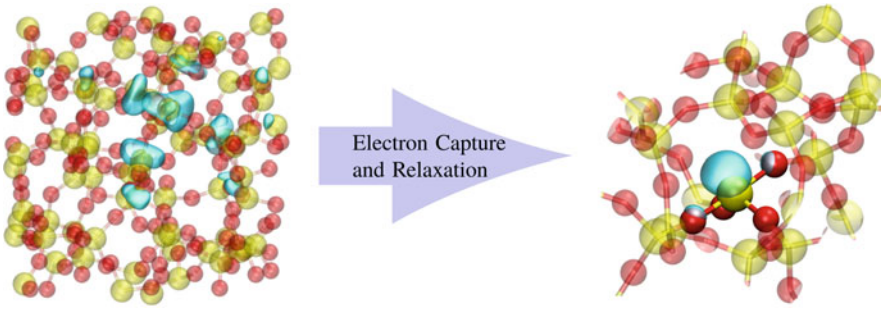

Fig. 14 Intrinsic electron trapping in a-SiO_2. **Left:** The LUMO is partially localized at certain sites in the structure. **Right:** Upon electron injection this orbital is filled and collapses onto a single Si atom. Reproduced from [105]

as shown in Fig. 14 (right). This structural relaxation is accompanied by a large energy gain resulting in a deep electron trap level on average 3.17 eV below the SiO_2 conduction band. It was further shown that the additional electron always spontaneously localizes at sites with O–Si–O angles exceeding 132°. Based on molecular dynamic models, the concentration of such sites was estimated to be around 4×10^{19} cm^{-3}, which is in excellent agreement with the experimentally observed trap density at this position in the bandgap.

For the sake of completeness it should be mentioned that intrinsic hole trapping was also observed in a-SiO_2 [106]. However, spectroscopic studies [107] together with later DFT investigations [108] suggest a hole trap level deep below the Si valence band. It can thus be assumed that intrinsic hole trapping does not contribute to NBTI or RTN in Si/SiO_2 based devices.

5.4 Comparison to Experimental Data

Due to the technological importance of SiO_2 in microelectronics and optics, defects in this material have been studied extensively both in experiment and theory. Here we compare the results from various DFT investigations for the aforementioned defect candidates with experimentally observed defect bands in devices with an a-SiO_2 oxide. In this discussion we will focus on comparisons to easily accessible quantities like thermodynamic trap levels and activation energies for charge transfer from electrical measurements. Detailed discussions on other parameters within the 4-state model like thermal barriers or relative stabilities can be found in [66, 72, 92].

Trap Level Distributions

Efforts were made to reduce the modeling complexity within the 4-state model, while at the same time keeping most of its predictive capabilities and capture the

essence of underlying defect physics. This resulted in an effective 2-state model implemented in a Compact-Physics framework (Comphy [83]). Based on electrical MSM sequences defect bands for NBTI and PBTI degradation were extracted for multiple commercial device architectures within this framework. A comparison between DFT calculations and the resulting experimental trap levels for the 28 nm foundry planar technology is shown in Fig. 15. In the case of NBTI degradation it can be seen that the hydrogen-related defects HB and H-E′ act as hole traps close to the Si valence band in good agreement with the experimental evidence. Although the OV defect can capture holes as discussed in Sect. 5.1, the resulting trap level is far too deep to explain the observed NBTI degradation. Under typical bias conditions this defect type is mostly neutral and thus does not interfere with the device electrostatics. The same holds true for intrinsic hole traps. Note that in order to be most consistent with the 2-state model used in Comphy, in the comparison to DFT calculations only OV, HB and H-E′ defects were considered which also showed an effective 2-state character [66].

PBTI degradation in Si/SiO_2-based devices is very weak and difficult to measure accurately. Thus the extracted experimental electron trap levels have some uncertainty and are drawn as dashed lines. Figure 15 shows that intrinsic electron traps described in Sect. 5.3 may be responsible for this weak observed trap band. The hydrogen-related defect candidates discussed in Sect. 5.2 are known to be

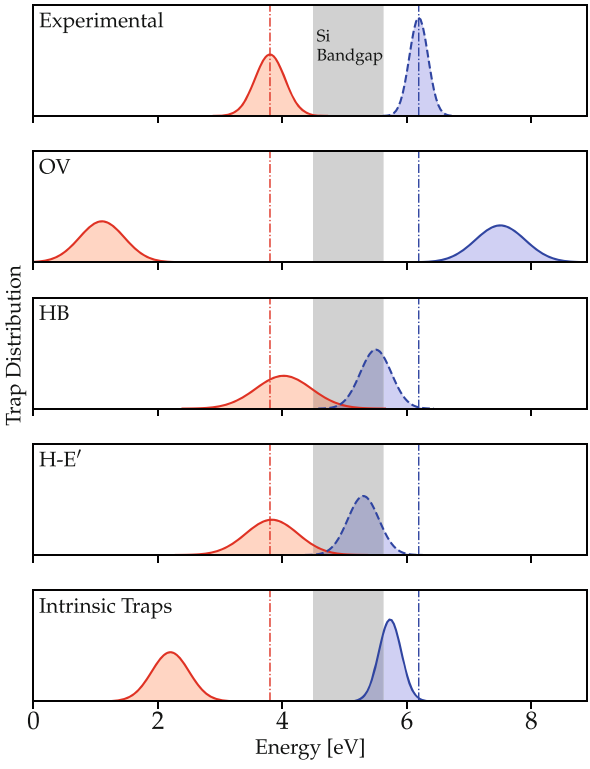

Fig. 15 Schematic trap level distributions from experiments and DFT predictions for various defect candidates in a-SiO_2. The shaded area marks the position of the Si bandgap. Red and blue lines indicate the distribution of hole and electron traps, respectively. The dashed lines show distributions from insufficient data sets, which may need further investigation. Sources for hole and electron trapping, respectively: Experimental [83], OV [66, 109], H-E′ [66, 100], HB [66, 100], intrinsic traps [105, 108]. Note that in the case of intrinsic traps the relaxed defect orbital energy was plotted, since the thermodynamic trap level was not calculated in these studies. However, these values give an estimate of the corresponding trap levels

able of capturing an electron [100], the resulting trap level are also lying near the experimental range. However, since these studies focused primarily on hole trapping mechanisms, only little information on electron trapping is available for these defects. Although PBTI is rather unimportant in Si/SiO_2 devices, the extracted defect band may play an important role in SiC/SiO_2 device degradation due to the different band alignments. A detailed theoretical study on electron traps in SiO_2 is thus desired in future works to better understand the degradation mechanisms in these devices.

Finally it should be emphasized that calculations of defect trap levels from DFT depend on the used XC functionals and are strongly affected by the resulting bandgap. The given distributions should therefore be considered as *qualitative* guidelines for the identification of possible defect candidates rather than a quantitative analysis. In order to get more accurate estimates for charge trap levels, higher levels of theory like the GW approximation [110] could be used to calculate correction terms for the studied defects.

Defect Activation Energies

Although the position of the charge trap level is an important indicator to judge whether or not a given defect candidate can explain the experimental data, it only provides the average occupancy in thermal equilibrium at a given gate bias. However, there is no information about the time scales on which a charge transition would occur. Using the transition rates of NMP theory (Eq. 29) together with the harmonic approximation shown in Fig. 10 allows the extraction of capture and emission activation energies for a given defect candidate from DFT simulations. These quantities are useful since they are also accessible from experiments and do not depend on the defect position relative to the interface, which would be meaningless in bulk oxide simulations. Figure 16 shows the distribution of

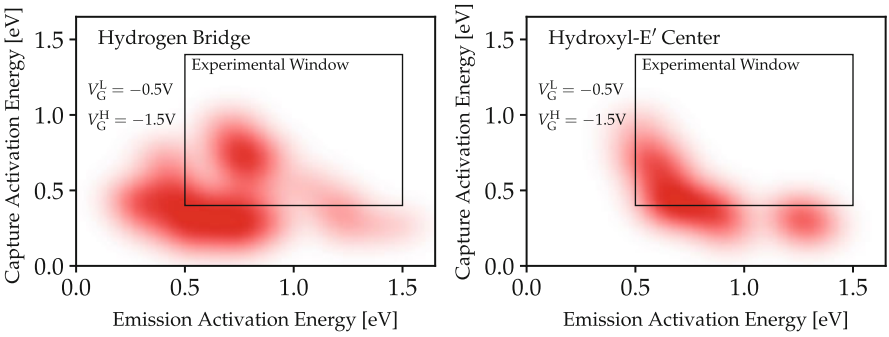

Fig. 16 Distributions of hole capture and emission activation energies for the hydrogen bridge and hydroxyl-E′ center. Significant portions of the distributions lie within the experimental window, indicating that these defects are active under typical bias conditions. Reproduced from [92]

activation energies for the hydrogen bridge and the hydroxyl-E′ center alongside the experimental window in which RTN and BTI can be observed. As can be seen, a considerable amount of these defect candidates lie within this window, indicating that they are visible during RTS or TDDS measurements [92]. These findings suggest that hydrogen-related defects are likely candidates for hole trapping in SiO_2. Although activation energies for intrinsic electron traps are not available, based on their relaxation energy of 0.8 eV one might speculate that these sites could act as fast electron traps. However, this needs to be investigated in future works.

Defect Volatility

Defects in a-SiO_2 are known to frequently disappear during TDDS measurements and stay inactive for a certain amount of time [111]. Such a defect behavior is termed volatility. Assuming a first-order thermally activated process as the underlying cause of volatility, the corresponding activation energies can be estimated by an Arrhenius law. Given an inactive timespan of at least 1200 s at room temperature during experiments results in an activation energy of around $E_A^{vol} \approx 1.0$ eV. Furthermore measurements on large-area devices with varying H content suggest a reaction involving hydrogen as the root cause of volatility [112]. It is therefore worth taking a closer look at the kinetics of hydrogen, especially the repassivation of the HB and HE center defects. In the following the findings of our previous works [72, 113] regarding the role of hydrogen in defect volatility are summarized.

In the case of the hydrogen bridge, volatility is expected to occur when the H is released and an oxygen vacancy is formed. Since the Si–H bond is very strong, the thermal barrier for the repassivation of HB defects is rather high. Nudged elastic band calculations for the dissociation of the Si–H bond in the positive charge state at multiple defect sites showed that there is a minimal barrier of 2.6 eV for this reaction. Similar findings also hold true in the neutral charge state. Such high barriers clearly indicate that HB defects cannot account for the observed volatility. On the other hand, dissociation of a neutral H-E′ center has a reaction barrier of 1.66 eV on average, with a standard deviation of 0.37 eV. Although the barrier is smaller than for the HB defect, this process still does not provide a satisfactory explanation for defect volatility. However, it has been demonstrated, that the H^+ ion of the positive H-E′ center can dissociate with barriers sometimes even lower than 1.0 eV. In this case, the H^+ ion could hop to a nearby O site, forming a new state termed 0^+ as shown in Fig. 17. It was found that the states $2'$ and 0^+ are energetically similar, leading to comparable barriers for the forward and backward reaction. However, since in a-SiO_2 all O sites differ from each other, the new state 0^+ may not support the formation of a new electrically active H-E′ center, which leads to the disappearance of the defect during measurements. Since volatility is frequently observed in experiments, these theoretical findings suggest that the H-E′ center might be a better defect candidate to explain the measured trap behavior compared to the HB.

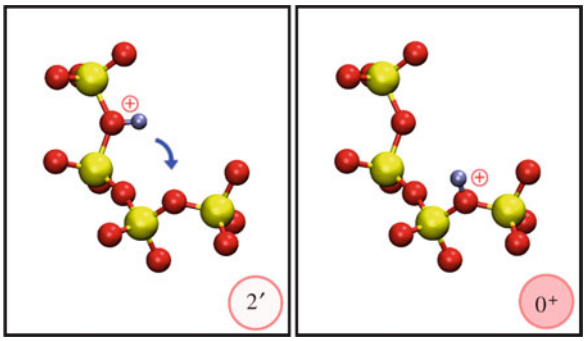

Fig. 17 Possible mechanism behind defect volatility. The H^+ ion of the positive hydroxyl-E′ center can hop to nearby O sites with barriers as low as 1.0 eV. This is possible since the ion is only bound via Coulomb attraction and therefore no chemical bond breaking is required during this process [72]

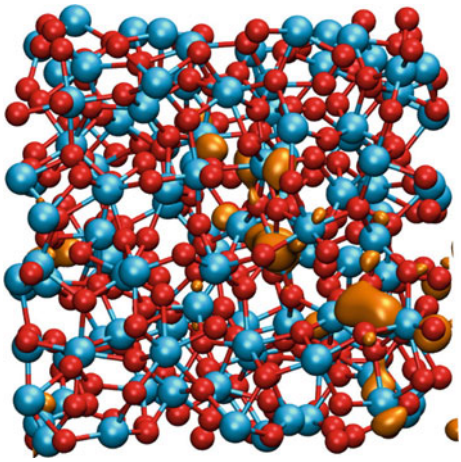

Fig. 18 Periodic a-HfO_2 model with 324 atoms. Most O atoms within the structure are threefold-coordinated, indicating a strong ionic binding component, which is absent in a-SiO_2. The majority of Hf atoms are 6-fold coordinated; however, a significant portion is also 5- or 7-coordinated. The orange bubble represents the partially localized LUMO, showing precursor sites for intrinsic charge trapping. Reproduced from [114]

6 Defects in Amorphous HfO_2

Although SiO_2 was the primary dielectric in microelectronics for decades, further downscaling of devices required the use of novel gate dielectrics. For example, the decreasing size of transistors also demands a reduction of the effective oxide thickness in order to keep the electrostatic control over the channel. However, such thin oxides have an increased leakage current, which drastically increases the power consumption and requirements for heat dissipation. To overcome this scaling issue, a thick layer of a high-κ material like hafnia (HfO_2) is used to decrease the leakage current while keeping control over the channel. HfO_2 can exist in a crystalline cubic phase and a metastable amorphous phase. HfO_2, together with other metal oxides like ZrO_2 and Al_2O_3, is a non-glass forming oxide. This implies that, contrary to SiO_2, the coordination numbers and oxidation states vary throughout the structure for the same kind of atoms. Due to the higher degree of disorder compared to a-SiO_2, see Fig. 18, it is suspected that intrinsic charge trapping at under- or overcoordinated sites plays a fundamental role for BTI and RTN in these materials [114]. Non-glass forming oxide films on substrates tend to be less stable than comparable SiO_2 films

and can undergo structural transformations during processing steps. For example, HfO_2 films are known to partially crystallize during annealing [115]. Due to this additional structural uncertainty, atomistic modeling of non-glass forming metal oxides is particularly challenging. Devices with high-κ dielectrics like HfO_2 or other amorphous metal oxides are significantly affected by PBTI degradation, indicating that electron trapping is more pronounced in these materials than hole trapping. Although the density of hole traps can be rather high in HfO_2, the energetic position relative to the substrate valence band edge render them mostly inactive in common gate stack structures like $HfO_2/SiO_2/Si$ [83].

6.1 Oxygen Vacancies

Similar to SiO_2, oxygen vacancies can naturally form in a-HfO_2 due to local oxygen deficiency during deposition. Oxygen vacancies in a-HfO_2 can either form at two-, three-, or four-coordinated O sites. They are known to exist in neutral, positive, and negative states. Due to the ionic bonding character in HfO_2, oxygen vacancies behave like F-centers in ionic crystals, i.e., additional charges are strongly localized within the vacancy [116]. Since oxygen vacancies can also exist in negative charge states it was assumed that they could be responsible for the high density of electron traps observed in high-κ devices. However, recent theoretical studies [117] showed that the corresponding trap level $E_T^{0/-}$ lies closely below the HfO_2 conduction band and is therefore too shallow to explain the experimental findings based on optical [117] and electrical [83] measurements. As shown in Fig. 19, the positively charged vacancy is thermodynamically stable for Fermi levels below $E_F < 4.3\,\text{eV}$. This results in a hole trap level $E_T^{0/+}$ above the Si conduction band edge. The majority of these vacancies will therefore form fixed positive oxide charges.

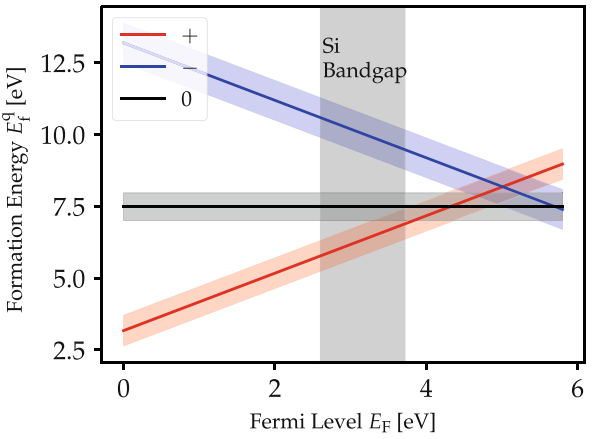

Fig. 19 Formation energies for the oxygen vacancy in a-HfO_2. The spreading of formation energies due to the amorphous host is indicated by the shaded strips. Adapted from [117]

Beside their possible role as charge traps, oxygen vacancies are also investigated as a potential cause of resistive switching in novel hafnia-based RRAM devices. It has been demonstrated recently that electron injection in HfO_2 can create Frenkel-pairs consisting of oxygen vacancies and interstitial O^{-2} ions. Furthermore, preexisting oxygen vacancies act as electron traps and can facilitate the formation of these Frenkel-pairs nearby, resulting in a stable divacancy [118]. This process suggests a possible aggregation of oxygen vacancies, which leads to a significant reduction of resistivity due to formation of a conductive filament.

6.2 *Intrinsic Charge Trapping*

Numerous studies [83, 117] clearly show that electron trapping characteristics in HfO_2 have a pronounced dependence on the chemical details of film deposition as well as the parameters during annealing. These findings suggest electron traps that are sensitive to the phase of the oxide film, e.g., amorphous or crystalline. A possible explanation for these electron traps was proposed in [119, 120]. Based on their theoretical investigations the authors proposed that electron trapping could take place at intrinsic sites similar to the process already discussed for a-SiO_2. In the case of a-HfO_2, undercoordinated Hf-ions or elongated Hf–O bonds serve as precursor sites. Trapped electrons at such sites will be highly localized at two or three Hf atoms as shown in Fig. 20 (left). Additionally, the d-orbitals of the involved Hf atoms also carry substantial parts of the excess electron as indicated by the ring-shaped charge distributions. The extra electron leads to a distortion, where the Hf cations are pulled towards the trapped charge distribution, whereas the O anions are pushed outwards. These electron traps are therefore called polarons due to similarities with the identically named self-trapped charges in crystals. Contrary to crystalline HfO_2, the formation of polarons in a-HfO_2 is accompanied by a large relaxation energy of 0.8 eV on average, which makes electron polarons stable even at room temperature.

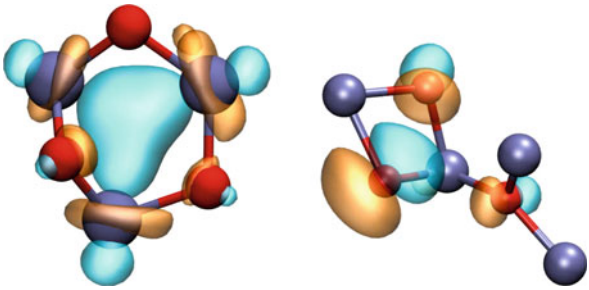

Fig. 20 Charge distributions of intrinsic traps in a-HfO_2. **Left:** In an electron polaron the additional charge is shared between two or three Hf atoms. The ring-shaped distributions indicate a participation of the Hf d-orbitals. **Right:** A hole polaron localizes on several O atoms near the trapping site. Reproduced from [114]

Similarly, holes have been demonstrated to localize at certain O atoms, forming a so-called hole polaron as shown in Fig. 20 (right) with a relaxation energy of 0.7 eV [119].

6.3 Trap Level Distributions

Similar to Sect. 5.4 we now compare the resulting trap levels of the discussed defects with the fitted model parameters from experiments using the Comphy framework. As shown in Fig. 21, the experimentally observed hole trap level in a-HfO_2 lies within the Si bandgap. This explains the rather weak NBTI response from hafnia in ordinary $HfO_2/SiO_2/Si$ stacks. However, the response of this defect band is much larger when a few additional layers of Al_2O_3 are deposited on the stack due to different energetic alignment with respect to the gate Fermi level [83]. Electrical characterizations on $HfO_2/SiO_2/Si$ stacks show a large hole trap density in the HfO_2 region [83], suggesting HfO_2 related defects as its origin. In contrast, other investigations found that the measured hole trap density is nearly unaffected by the thickness of the deposited HfO_2 layer, indicating a dominant role of defect states at the HfO_2/SiO_2 interface for the NBTI phenomenon [118, 121]. As can be seen in Fig. 21, DFT calculations suggest that the hole trap band in a-HfO_2 consists of intrinsic hole polarons, whereas the oxygen vacancy clearly is not a suitable candidate due to its very high trap level. This finding might also give an explanation for the experimental discrepancies regarding hole trapping in hafnia. Hole polarons require an amorphous oxide in order to be stable. During annealing steps the HfO_2 layer tends to partially crystallize, leading to different experimental estimates for the trap location depending on annealing conditions.

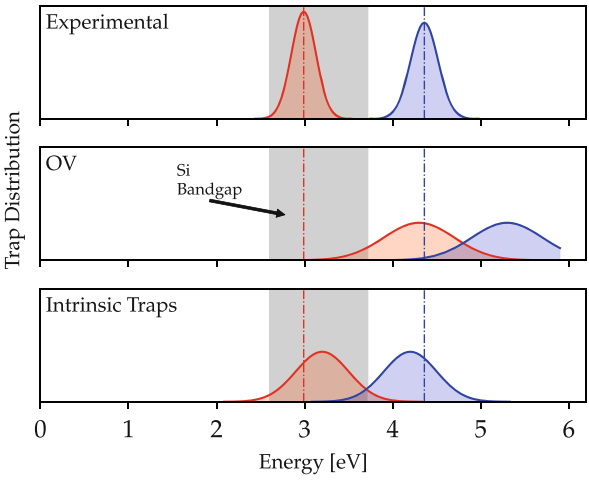

Fig. 21 Schematic trap level distributions from experiments and DFT predictions for defect candidates in a-HfO_2, similar to Fig. 15. Sources: Experimental [83], OV [117], intrinsic traps [119]. Note that in the case of intrinsic traps the relaxed defect orbital energy was plotted, since the thermodynamic trap level was not calculated in these studies. However, these values give an estimate of the corresponding trap levels

A similar picture can be drawn for the measured electron trap band. Here the predicted electron trap level for the oxygen vacancy is very close to the HfO_2 conduction band and is thus too shallow to account for the experimental data. However, DFT predictions for electron polarons match the measured trap levels perfectly. This finding is also supported by time-dependent DFT studies on the photo-absorption spectra of electron polarons, which fits nicely to optical measurements in a-HfO_2 samples [114]. In summary, all these findings lead to the conclusion that intrinsic electron and hole polarons play a fundamental role in the BTI degradation mechanism of hafnia-based devices.

7 Summary and Outlook

In this chapter we have investigated the microscopic structure of possible defect candidates responsible for RTN and BTI in SiO_2 and HfO_2, two of the most important gate oxide materials in microelectronics. Using molecular dynamics together with the melt-quench procedure allows for the realistic atomic modeling of amorphous gate oxides. Density functional theory can then be used to create defects inside these model structures and study their behavior from first principles. In combination with the 4-state NMP model, important defect parameters like the thermodynamic trap level or charge transition barriers and activation energies can be extracted from DFT. These parameters are also accessible from experimental measurement techniques like the analysis of RTN signals or time-dependent defect spectroscopy. This allows for the identification of relevant defects and might lead to strategies for improving device reliability.

Contrary to previous assumptions, we showed that RTN and NBTI in devices with SiO_2 gate oxide cannot be explained by oxygen vacancies since they stay mostly inactive under typical operating conditions. However, hydrogen-related defects like the hydrogen bridge and the hydroxyl-E' center are likely acting as hole traps. Furthermore it was demonstrated that strained structures within amorphous silica act as intrinsic electron traps. Although there is a need for further investigations, the available data suggests that these intrinsic traps might be responsible for PBTI degradation, which is particularly important for power devices based on SiC.

High-κ materials like HfO_2 are non-glass forming metal oxides. Due to the high degree of disorder in their amorphous phase, intrinsic charge trapping seems to play a major role for device reliability in these materials. It was shown that intrinsic hole and electron traps in HfO_2 match the experimental charge trap levels nearly perfectly. However, so far it is unknown if these intrinsic traps possess metastable states as required by the 4-state model. Also, the charge trapping dynamics of these sites need further investigation.

All results presented in this work are obtained from bulk oxide models. This is a frequently used and convenient model simplification. However, many defects are expected to be near the interface, where the assumption of bulk-like oxide properties

is likely breaking down. For example, the oxide near the interface is usually strained and might not be stoichiometric. In order to study the impact of these effects on defects, theoretical studies on interface models should be conducted in the future.

References

1. M. Kirton, M. Uren, Noise in solid-state microstructures: a new perspective on individual defects, interface states and low-frequency (1/f) noise. Adv. Phys. **38**(4), 367–468 (1989)
2. Y. Miura, Y. Matukura, Investigation of silicon-silicon dioxide interface using MOS structure. Jpn. J. Appl. Phys. **5**(2), 180 (1966)
3. T. Grasser, K. Rott, H. Reisinger, M. Waltl, J. Franco, B. Kaczer, A unified perspective of RTN and BTI, in *2014 IEEE International Reliability Physics Symposium* (2014), pp. 4A.5.1–4A.5.7
4. M. Chudzik, B. Doris, R. Mo, J. Sleight, E. Cartier, C. Dewan, D. Park, H. Bu, W. Natzle, W. Yan, C. Ouyang, K. Henson, D. Boyd, S. Callegari, R. Carter, D. Casarotto, M. Gribelyuk, M. Hargrove, W. He, Y. Kim, B. Linder, N. Moumen, V.K. Paruchuri, J. Stathis, M. Steen, A. Vayshenker, X. Wang, S. Zafar, T. Ando, R. Iijima, M. Takayanagi, V. Narayanan, R. Wise, Y. Zhang, R. Divakaruni, M. Khare, T.C. Chen, High-performance high- amp metal gates for 45nm CMOS and beyond with gate-first processing, in *2007 IEEE Symposium on VLSI Technology* (2007), pp. 194–195
5. F. Schanovsky, O. Baumgartner, V. Sverdlov, T. Grasser, J. Comput. Electron. **11**(3), 218–224 (2012)
6. T. Grasser, Stochastic charge trapping in oxides: from random telegraph noise to bias temperature instabilities. Microelectron. Reliab. **52**(1), 39–70 (2012)
7. H. Miki, N. Tega, M. Yamaoka, D.J. Frank, A. Bansal, M. Kobayashi, K. Cheng, C.P. D'Emic, Z. Ren, S. Wu, J.B. Yau, Y. Zhu, M.A. Guillorn, D.G. Park, W. Haensch, E. Leobandung, K. Torii, Statistical measurement of random telegraph noise and its impact in scaled-down high-k metal-gate MOSFETs, in *2012 International Electron Devices Meeting* (2012), pp. 19.1.1–19.1.4
8. T. Grasser, H. Reisinger, P.-J. Wagner, B. Kaczer, Time-dependent defect spectroscopy for characterization of border traps in metal-oxide-semiconductor transistors. Phys. Rev. B **82**, 245318 (2010)
9. T. Grasser, P. Wagner, P. Hehenberger, W. Gos, B. Kaczer, A rigorous study of measurement techniques for negative bias temperature instability, in *2007 IEEE International Integrated Reliability Workshop Final Report* (2007), pp. 6–11
10. B. Stampfer, A. Grill, M. Waltl, Advanced electrical characterization of single oxide defects utilizing noise signals, in *Noise in Nanoscale Semiconductor Devices*, ed. by T. Grasser (Springer, Cham, 2019). https://doi.org/10.1007/978-3-030-37500-3_7
11. P. Lenahan, Dominating defects in the MOS system: P_b and E' centers, in *Defects in Microelectronic Materials and Devices*, ed. by D. Fleetwood, R. Schrimpf, S. Pantelides (Taylor and Francis/CRC Press, Boca Raton, 2008)
12. A. Stesmans, V.V. Afanas'ev, Electron spin resonance features of interface defects in thermal (100) Si/SiO_2. J. Appl. Phys. **83**(5), 2449–2457 (1998)
13. J.F. Conley, P.M. Lenahan, Room temperature reactions involving silicon dangling bond centers and molecular hydrogen in amorphous SiO_2 thin films on silicon, Appl. Phys. Lett. **62**(1), 40–42 (1993)
14. A.T. Krishnan, S. Chakravarthi, P. Nicollian, V. Reddy, S. Krishnan, Negative bias temperature instability mechanism: the role of molecular hydrogen. Appl. Phys. Lett. **88**(15), 153518 (2006)

15. T. Grasser, B. Kaczer, W. Goes, An energy-level perspective of bias temperature instability, in *2008 IEEE International Reliability Physics Symposium* (2008), pp. 28–38
16. T. Aichinger, S. Puchner, M. Nelhiebel, T. Grasser, H. Hutter, Impact of hydrogen on recoverable and permanent damage following negative bias temperature stress, in *2010 IEEE International Reliability Physics Symposium* (2010), pp. 1063–1068
17. S. Mohr, L.E. Ratcliff, L. Genovese, D. Caliste, P. Boulanger, S. Goedecker, T. Deutsch, Accurate and efficient linear scaling DFT calculations with universal applicability. Phys. Chem. Chem. Phys. **17**, 31360–31370 (2015)
18. M. Born, R. Oppenheimer, Zur quantentheorie der molekeln. Ann. Phys. **389**(20), 457–484 (1927)
19. A. Szabo, *Modern Quantum Chemistry: Introduction to Advanced Electronic Structure Theory* (McGraw-Hill, New York, 1989)
20. P. Hohenberg, W. Kohn, Inhomogeneous electron gas. Phys. Rev. **136**, B864–B871 (1964)
21. E. Engel, *Density Functional Theory: An Advanced Course* (Springer, Berlin, 2011)
22. W. Kohn, L.J. Sham, Self-consistent equations including exchange and correlation effects. Phys. Rev. **140**, A1133–A1138 (1965)
23. P.A.M. Dirac, Note on exchange phenomena in the Thomas atom. Math. Proc. Cambridge Philos. Soc. **26**(3), 376–385 (1930)
24. D.M. Ceperley, B.J. Alder, Ground state of the electron gas by a stochastic method. Phys. Rev. Lett. **45**, 566–569 (1980)
25. P.P. Rushton, Towards a non-local density functional description of exchange and correlation. PhD Thesis, University of Durham, 2002
26. J.P. Perdew, K. Burke, M. Ernzerhof, Generalized gradient approximation made simple [Phys. Rev. Lett. 77, 3865 (1996)]. Phys. Rev. Lett. **78**, 1396–1396 (1997)
27. J.P. Perdew, J.A. Chevary, S.H. Vosko, K.A. Jackson, M.R. Pederson, D.J. Singh, C. Fiolhais, Atoms, molecules, solids, and surfaces: applications of the generalized gradient approximation for exchange and correlation. Phys. Rev. B **46**, 6671–6687 (1992)
28. D.C. Langreth, M.J. Mehl, Beyond the local-density approximation in calculations of ground-state electronic properties. Phys. Rev. B **28**, 1809–1834 (1983)
29. A.D. Becke, A new mixing of Hartree-Fock and local density-functional theories. J. Chem. Phys. **98**(2), 1372–1377 (1993)
30. A.J. Garza, G.E. Scuseria, Predicting band gaps with hybrid density functionals. J. Phys. Chem. Lett. **7**, 08 (2016)
31. J. Heyd, G.E. Scuseria, M. Ernzerhof, Hybrid functionals based on a screened coulomb potential. J. Chem. Phys. **118**(18), 8207–8215 (2003)
32. J.P. Perdew, M. Ernzerhof, K. Burke, Rationale for mixing exact exchange with density functional approximations. J. Chem. Phys. **105**(22), 9982–9985 (1996)
33. A.D. Becke, Density functional thermochemistry. III. The role of exact exchange. J. Chem. Phys. **98**(7), 5648–5652 (1993)
34. M. Guidon, J. Hutter, J. VandeVondele, Auxiliary density matrix methods for Hartree-Fock exchange calculations. J. Chem. Theory Comput. **6**(8), 2348–2364 (2010). PMID: 26613491
35. V.B. Sulimov, P.V. Sushko, A.H. Edwards, A.L. Shluger, A.M. Stoneham, Asymmetry and long-range character of lattice deformation by neutral oxygen vacancy in α-quartz. Phys. Rev. B **66**, 024108 (2002)
36. A.-M. El-Sayed, Atomistic modelling of charge trapping defects in silicon dioxide. PhD thesis, University College London, 2015
37. D. Muñoz Ramo, J.L. Gavartin, A.L. Shluger, G. Bersuker, Spectroscopic properties of oxygen vacancies in monoclinic HfO_2 calculated with periodic and embedded cluster density functional theory. Phys. Rev. B **75**, 205336 (2007)
38. P.E. Blöchl, J.H. Stathis, Hydrogen electrochemistry and stress-induced leakage current in silica. Phys. Rev. Lett. **83**, 372–375 (1999)
39. A.-M. El-Sayed, M.B. Watkins, T. Grasser, V.V. Afanas'ev, A.L. Shluger, Hydrogen-induced rupture of strained Si–O bonds in amorphous silicon dioxide. Phys. Rev. Lett. **114**, 115503 (2015)

40. T. Schlick, *Molecular Modeling and Simulation: An Interdisciplinary Guide* (Springer Science+Business Media, LLC, New York 2010)
41. T.P. Senftle, S. Hong, M.M. Islam, S.B. Kylasa, Y. Zheng, Y.K. Shin, C. Junkermeier, R. Engel-Herbert, M.J. Janik, H.M. Aktulga, T. Verstraelen, A. Grama, A.C.T. van Duin, The ReaxFF reactive force-field: development, applications and future directions. npj Comput. Mater. **2**, 15011 EP (2016). Review Article
42. G. Broglia, G. Or, L. Larcher, M. Montorsi, Molecular dynamics simulation of amorphous HfO_2 for resistive RAM applications. Modell. Simul. Mater. Sci. Eng. **22**, 065006 (2014)
43. S.R. Elliott, *Physics of Amorphous Materials* (Longman, New York, 1984)
44. D. Price, J. Carpenter, Scattering function of vitreous silica. J. Non Cryst. Solids **92**(1), 153–174 (1987)
45. R. Martin, *Electronic Structure: Basic Theory and Practical Methods* (Cambridge University Press, Cambridge, 2008)
46. P. McMillan, B. Piriou, R. Couty, A Raman study of pressure-densified vitreous silica. J. Chem. Phys. **81**(10), 4234–4236 (1984)
47. D.R. Fredkin, A. Komornicki, S.R. White, K.R. Wilson, Ab initio infrared and Raman spectra. J. Chem. Phys. **78**(12), 7077–7092 (1983)
48. B. Kaduk, T. Kowalczyk, T. Van Voorhis, Constrained density functional theory. Chem. Rev. **112**(1), 321–370 (2012). PMID: 22077560
49. C.G. Van de Walle, J. Neugebauer, First-principles calculations for defects and impurities: applications to III-Nitrides. J. Appl. Phys. **95**(8), 3851–3879 (2004)
50. S. Lany, A. Zunger, Assessment of correction methods for the band-gap problem and for finite-size effects in supercell defect calculations: case studies for ZnO and GaAs. Phys. Rev. B **78**, 235104 (2008)
51. C. Freysoldt, J. Neugebauer, C.G. Van de Walle, Fully ab initio finite-size corrections for charged-defect supercell calculations. Phys. Rev. Lett. **102**, 016402 (2009)
52. H.-P. Komsa, T.T. Rantala, A. Pasquarello, Finite-size supercell correction schemes for charged defect calculations. Phys. Rev. B **86**, 045112 (2012)
53. A.-M. El-Sayed, Y. Wimmer, W. Goes, T. Grasser, V.V. Afanas'ev, A.L. Shluger, Theoretical models of hydrogen-induced defects in amorphous silicon dioxide. Phys. Rev. B **92**, 014107 (2015)
54. K.O. Jeppson, C.M. Svensson, Negative bias stress of MOS devices at high electric fields and degradation of MNOS devices. J. Appl. Phys. **48**(5), 2004–2014 (1977)
55. M. Houssa, M. Aoulaiche, S. De Gendt, G. Groeseneken, M.M. Heyns, A. Stesmans, Reaction-dispersive proton transport model for negative bias temperature instabilities. Appl. Phys. Lett. **86**(9), 093506 (2005)
56. F. Schanovsky, T. Grasser, On the microscopic limit of the RD model, in *Bias Temperature Instability for Devices and Circuits*, ed. by T. Grasser (Springer, New York, 2014)
57. R.N. Hall, Electron-hole recombination in germanium. Phys. Rev. **87**, 387–387 (1952)
58. W. Shockley, W.T. Read, Statistics of the recombinations of holes and electrons. Phys. Rev. **87**, 835–842 (1952)
59. A. McWorther, 1/f noise and related surface effects in germanium. Sc.D Thesis, Massachusetts Institute of Technology, 1955
60. F. Schanovsky, W. Gös, T. Grasser, An advanced description of oxide traps in MOS transistors and its relation to DFT. J. Comput. Electron. **9**, 135–140 (2010)
61. F. Schanovsky, W. Gös, T. Grasser, Multiphonon hole trapping from first principles. J. Vac. Sci. Technol. B **29**(1), 01A201 (2011)
62. F. Schanovsky, O. Baumgartner, V. Sverdlov, T. Grasser, A multi scale modeling approach to non-radiative multi phonon transitions at oxide defects in MOS structures. J. Comput. Electron. **11**, 218–224 (2012)
63. K. Huang, A. Rhys, Theory of light absorption and non-radiative transitions in F-centres. Proc. Roy. Soc. Lond. A: Math. Phys. Eng. Sci. **204**(1078), 406–423 (1950)
64. C.H. Henry, D.V. Lang, Nonradiative capture and recombination by multiphonon emission in GaAs and GaP. Phys. Rev. B **15**, 989–1016 (1977)

65. W. Goes, F. Schanovsky, T. Grasser, Advanced modeling of oxide defects, in *Bias Temperature Instability for Devices and Circuits*, ed. by T. Grasser (Springer, New York, 2014)
66. W. Goes, Y. Wimmer, A.-M. El-Sayed, G. Rzepa, M. Jech, A. Shluger, T. Grasser, Identification of oxide defects in semiconductor devices: a systematic approach linking DFT to rate equations and experimental evidence. Microelectron. Reliab. **87**, 286–320 (2018)
67. T. Grasser, H. Reisinger, P. Wagner, B. Kaczer, F. Schanovsky, W. Goes, The time dependent defect spectroscopy (TDDS) for the characterization of the bias temperature instability, in *Proceedings of the International Reliability Physics Symposium* (2010), pp. 16–25
68. M. Waltl, G. Rzepa, A. Grill, W. Gös, J. Franco, B. Kaczer, L. Witters, J. Mitard, N. Horiguchi, T. Grasser, Superior NBTI in high-k SiGe transistors–part I: experimental. IEEE Trans. Electron Devices **64**(5), 2092–2098 (2017)
69. M. Waltl, G. Rzepa, A. Grill, W. Gös, J. Franco, B. Kaczer, L. Witters, J. Mitard, N. Horiguchi, T. Grasser, Superior NBTI in high-k SiGe transistors–part II: theory. IEEE Trans. Electron Devices **64**(5), 2099–2105 (2017)
70. F. Schanovsky, Atomistic modeling in the context of the bias temperature instability. Ph.D Thesis, TU Wien, 2013
71. W. Goes, Hole trapping and the negative bias temperature instability. Ph.D Thesis, TU Wien, 2011
72. Y. Wimmer, A.-M. El-Sayed, W. Gös, T. Grasser, A.L. Shluger, Role of hydrogen in volatile behaviour of defects in SiO_2-based electronic devices. Proc. Roy. Soc. A: Math. Phys. Eng. Sci. **472**(2190), 20160009 (2016)
73. H. Eyring, The activated complex in chemical reactions. J. Chem. Phys. **3**(2), 107–115 (1935)
74. M.G. Evans, M. Polanyi, Some applications of the transition state method to the calculation of reaction velocities, especially in solution. Trans. Faraday Soc. **31**, 875–894 (1935)
75. R. Fletcher, *Practical Methods of Optimization* (Wiley, Chichester, 1987)
76. H. Jónsson, G. Mills, K.W. Jacobsen, Nudged elastic band method for finding minimum energy paths of transitions, in *Classical and Quantum Dynamics in Condensed Phase Simulations* (World scientific, Singapore, 1998), pp. 385–404
77. Y. Wimmer, Hydrogen related defects in amorphous SiO_2 and the negative bias temperature instability. PhD Thesis, TU Vienna, E360, 2017
78. J. Franck, E.G. Dymond, Elementary processes of photochemical reactions. Trans. Faraday Soc. **21**, 536–542 (1926)
79. E. Condon, A theory of intensity distribution in band systems. Phys. Rev. **28**, 1182–1201 (1926)
80. J.F. Conley, P.M. Lenahan, W.F. McArthur, Preliminary investigation of the kinetics of postoxidation rapid thermal anneal induced hole-trap-precursor formation in microelectronic SiO_2 films. Appl. Phys. Lett. **73**(15), 2188–2190 (1998)
81. T. Tewksbury, Relaxation effects in MOS devices due to tunnel exchange with near-interface oxide traps. Ph.D Thesis, Massachusetts Institute of Technology, 1992
82. T. Chachiyo, J.H. Rodriguez, A direct method for locating minimum-energy crossing points (MECPs) in spin-forbidden transitions and nonadiabatic reactions. J. Chem. Phys. **123**(9), 094711 (2005)
83. G. Rzepa, J. Franco, B. O'Sullivan, A. Subirats, M. Simicic, G. Hellings, P. Weckx, M. Jech, T. Knobloch, M. Waltl, P.J. Roussel, D. Linten, B. Kaczer, T. Grasser, Comphy—a compact-physics framework for unified modeling of BTI. Microelectron. Reliab. **85**, 49–65 (2018)
84. K.L. Yip, W.B. Fowler, Electronic structure of E_1' centers in SiO_2. Phys. Rev. B **11**, 2327–2338 (1975)
85. E.P. O'Reilly, J. Robertson, Theory of defects in vitreous silicon dioxide. Phys. Rev. B **27**, 3780–3795 (1983)
86. J.K. Rudra, W.B. Fowler, F.J. Feigl, Model for the E_2' center in alpha quartz. Phys. Rev. Lett. **55**, 2614–2617 (1985)
87. M.K. Schurman, M. Tomozawa, Equilibrium oxygen vacancy concentrations and oxidant diffusion in germania, silica, and germania-silica glasses. J. Non-Cryst. Solids **202**(1), 93–106 (1996)

88. S. Mukhopadhyay, P.V. Sushko, A.M. Stoneham, A.L. Shluger, Modeling of the structure and properties of oxygen vacancies in amorphous silica. Phys. Rev. B **70**, 195203 (2004)
89. N. Richard, L. Martin-SaMOS, G. Roma, Y. Limoge, J.-P. Crocombette, First principle study of neutral and charged self-defects in amorphous SiO_2. J. Non-Cryst. Solids **351**(21), 1825–1829 (2005)
90. S. Pantelides, Z.-Y. Lu, C. Nicklaw, T. Bakos, S. Rashkeev, D. Fleetwood, R. Schrimpf, The E' center and oxygen vacancies in SiO_2. J. Non-Cryst. Solids **354**(2), 217–223 (2008). Physics of Non-Cryst. Solids 11.
91. F. Schanovsky, O. Baumgartner, W. Gös, T. Grasser, A detailed evaluation of model defects as candidates for the bias temperature instability, in *Proceedings of the International Conference on Simulation of Semiconductor Processes and Devices (SISPAD)* (2013), pp. 1–4
92. T. Grasser, W. Gös, Y. Wimmer, F. Schanovsky, G. Rzepa, M. Waltl, K. Rott, H. Reisinger, V.V. Afanas'Ev, A. Stesmans, A.-M. El-Sayed, A.L. Shluger, On the microscopic structure of hole traps in pMOSFETs, in *2014 IEEE International Electron Devices Meeting* (2014), pp. 530–533. Talk: International Electron Devices Meeting (IEDM), San Francisco (15 Dec 2014–17 Dec 2014)
93. P.M. Lenahan, J.P. Campbell, A.T. Krishnan, S. Krishnan, A model for NBTI in nitrided oxide MOSFETs which does not involve hydrogen or diffusion. IEEE Trans. Device Mater. Reliab. **11**, 219–226 (2011)
94. T. Aichinger, S. Puchner, M. Nelhiebel, T. Grasser, H. Hutter, Impact of hydrogen on recoverable and permanent damage following negative bias temperature stress, in *2010 IEEE International Reliability Physics Symposium* (2010), pp. 1063–1068
95. K. Kajihara, L. Skuja, M. Hirano, H. Hosono, Diffusion and reactions of hydrogen in F_2-laser-irradiated SiO_2 glass. Phys. Rev. Lett. **89**, 135507 (2002)
96. J. Godet, A. Pasquarello, Proton diffusion mechanism in amorphous SiO_2. Phys. Rev. Lett. **97**, 155901 (2006)
97. S.A. Sheikholeslam, H. Manzano, C. Grecu, A. Ivanov, Reduced hydrogen diffusion in strained amorphous SiO2: understanding ageing in MOSFET devices. J. Mater. Chem. C **4**, 8104–8110 (2016)
98. J. Isoya, J.A. Weil, L.E. Halliburton, EPR and ab initio SCF-MO studies of the Si-H-Si system in the E'_4 center of α-quartz. J. Chem. Phys. **74**(10), 5436–5448 (1981)
99. P.E. Blöchl, First-principles calculations of defects in oxygen-deficient silica exposed to hydrogen. Phys. Rev. B **62**, 6158–6179 (2000)
100. A.-M. El-Sayed, Y. Wimmer, W. Goes, T. Grasser, V.V. Afanas'ev, A.L. Shluger, Theoretical models of hydrogen-induced defects in amorphous silicon dioxide. Phys. Rev. B **92**, 014107 (2015)
101. C.M. Nelson, R.A. Weeks, Trapped electrons in irradiated quartz and silica: I, optical absorption. J. Am. Ceram. Soc. **43**(8), 396–399 (1960)
102. V.V. Afanas'ev, A. Stesmans, Interfacial defects in SiO_2 revealed by photon stimulated tunneling of electrons. Phys. Rev. Lett. **78**, 2437–2440 (1997)
103. N.S. Saks, A.K. Agarwal, Hall mobility and free electron density at the SiC/SiO_2 interface in 4H-SiC. Appl. Phys. Lett. **77**(20), 3281–3283 (2000)
104. A.A. Karpushin, A.N. Sorokin, V.A. Gritsenko, Si–Si bond as a deep trap for electrons and holes in silicon nitride. JETP Lett. **103**, 171–174 (2016)
105. A.-M. El-Sayed, M.B. Watkins, V.V. Afanas'ev, A.L. Shluger, Nature of intrinsic and extrinsic electron trapping in SiO_2. Phys. Rev. B **89**, 125201 (2014)
106. D.L. Griscom, Self-trapped holes in amorphous silicon dioxide. Phys. Rev. B **40**, 4224–4227 (1989)
107. Y. Sasajima, K. Tanimura, Optical transitions of self-trapped holes in amorphous SiO_2. Phys. Rev. B **68**, 014204 (2003)
108. A. Kimmel, P. Sushko, A. Shluger, Structure and spectroscopic properties of trapped holes in silica. J. Non-Cryst. Solids **353**(5), 599–604 (2007). SiO2, Advanced Dielectrics and Related Devices 6

109. D.Z. Gao, J. Strand, M.S. Munde, A.L. Shluger, Mechanisms of oxygen vacancy aggregation in SiO_2 and HfO_2. Front. Phys. **7**, 43 (2019)
110. F. Aryasetiawan, O. Gunnarsson, The GW method. Rep. Prog. Phys. **61**, 237–312 (1998)
111. T. Grasser, K. Rott, H. Reisinger, M. Waltl, P.-J. Wagner, F. Schanovsky, W. Gös, G. Pobegen, B. Kaczer, Hydrogen-related volatile defects as the possible cause for the recoverable component of NBTI, in *2013 International Electron Devices Meeting (IEDM) Technical Digest* (2013), pp. 409–412. Talk: International Electron Devices Meeting (IEDM), Washington (09 Dec 2013–11 Dec 2013)
112. T. Aichinger, M. Nelhiebel, S. Einspieler, T. Grasser, In situ poly heater-a reliable tool for performing fast and defined temperature switches on chip. IEEE Trans. Device Mater. Reliab. **10**, 3–8 (2010)
113. Y. Wimmer, W. Gös, A.-M. El-Sayed, A. L. Shluger, T. Grasser, A Density-functional study of defect volatility in amorphous silicon dioxide, in *Proceedings of the International Conference on Simulation of Semiconductor Processes and Devices (SISPAD)* (2015), pp. 44–47. Talk: International Conference on Simulation of Semiconductor Processes and Devices (SISPAD), Washington (09 Sep 2015–11 Sep 2015)
114. J. Strand, M. Kaviani, D. Gao, A.-M. El-Sayed, V.V. Afanas'ev, A.L. Shluger, Intrinsic charge trapping in amorphous oxide films: status and challenges. J. Phys.: Condens. Matter **30**, 233001 (2018)
115. F. Bohra, B. Jiang, J.-M. Zuo, Textured crystallization of ultrathin hafnium oxide films on silicon substrate. Appl. Phys. Lett. **90**(16), 161917 (2007)
116. A. Shluger, *Defects in Oxides in Electronic Devices* (Springer International Publishing, Cham, 2018), pp. 1–22
117. F. Cerbu, O. Madia, D.V. Andreev, S. Fadida, M. Eizenberg, L. Breuil, J.G. Lisoni, J.A. Kittl, J. Strand, A.L. Shluger, V.V. Afanas'ev, M. Houssa, A. Stesmans, Intrinsic electron traps in atomic-layer deposited HfO_2 insulators. Appl. Phys. Lett. **108**(22), 222901 (2016)
118. S.R. Bradley, G. Bersuker, A.L. Shluger, Modelling of oxygen vacancy aggregates in monoclinic HfO_2: can they contribute to conductive filament formation? J. Phys. Condens. Matter **27**, 415401 (2015)
119. M. Kaviani, J. Strand, V.V. Afanas'ev, A.L. Shluger, Deep electron and hole polarons and bipolarons in amorphous oxide. Phys. Rev. B **94**, 020103 (2016)
120. J. Strand, M. Kaviani, V.V. Afanas'ev, J.G. Lisoni, A.L. Shluger, Intrinsic electron trapping in amorphous oxide. Nanotechnology **29**, 125703 (2018)
121. V.V. Afanas'ev, A. Stesmans, Stable trapping of electrons and holes in deposited insulating oxides: Al_2O_3, ZrO_2, and HfO_2. J. Appl. Phys. **95**(5), 2518–2526 (2004)